
RICCI FLOW-GUIDED AUTOENCODERS IN LEARNING TIME-DEPENDENT DYNAMICS

Andrew Gracyk*

University of Illinois Urbana-Champaign

Abstract

We present a manifold-based autoencoder method for learning dynamics in time, notably partial differential equations (PDEs), in which the manifold latent space evolves according to Ricci flow. This can be accomplished by simulating Ricci flow in a physics-informed setting, and manifold quantities can be matched so that Ricci flow is empirically achieved. With our method, the manifold is discerned through the training procedure, while the latent evolution due to Ricci flow induces a more accommodating representation over static methods. We present our method on a range of experiments consisting of PDE data that encompasses desirable characteristics such as periodicity and randomness. By incorporating latent dynamics, we sustain a manifold latent representation for all values in the ambient PDE time interval. Furthermore, the dynamical manifold latent space facilitates qualities such as learning for out-of-distribution data, and robustness. We showcase our method by demonstrating these features.

1 Introduction

Data-driven techniques fueled by machine learning act as a meaningful conduit for exploring numerical-based approaches to partial differential equations (PDEs), such as in instances of finding solutions [23] [21] [38] [27] [8] [32] [35] [12]. A variety of frameworks have been developed with the purpose of finding approximations to time-dependent PDE solutions including encoder-decoder methods [22] [11] [39] [16]. Encoder-decoder methods are distinguished by a series of neural networks in which there exists an intermediate encoded space stage, which can be variously characterized, that is decoded to produce a PDE solution output. Encoder-decoder methods alone serve as a baseline method with limited properties, but by leveraging dynamic or geometric latent properties, they gain a general performance boost along with interpretability, extrapolation-ability, and robustness. Geometric dynamic variational autoencoders (GD-VAEs) [22] have shown great promise in learning discretized time-dependent dynamics, which are highlighted by an underlying latent space with either geometric features or dynamics in the latent space itself. We focus on an encoder-decoder method, emphasizing a low-dimensional manifold latent space which is imposed with dynamical evolution, that also holds the advantages that GD-VAEs achieve, including competitive error, generalization, extrapolation ability, and robustness.

A geometric flow, the foundation of our method, is a tool to perform dynamics among the manifold, in which we choose Ricci flow [34] [30] [7]. We first represent the initial PDE data in a domain to parameterize the manifold, which is then encoded directly to a point on the manifold. The points that compose this manifold evolve according to such a flow, in which we use a physics-informed neural network to simulate the evolution, matching quantities among the manifold to those that solve the physics-informed flow. Using neural networks to learn the manifold directly, we can learn implicit geometric features that harmonize with PDE data, observable from an error perspective.

Ricci flow is an example of an intrinsic geometric flow, meaning the relevant quantities computed in the PDE flow are inherent to the manifold itself [31], and so the manner in which it is embedded in space is not involved in the PDE computation and is otherwise irrelevant. An extrinsic geometric flow is a flow equation in which the embedding impacts the informational quantities used in the PDE, and so the embedding does indeed matter and is factored into

*Based on support from DIGIMAT with Grant No. 1922758

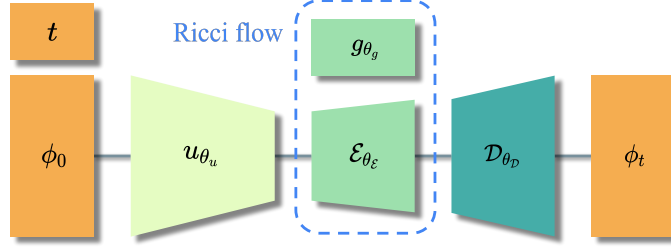


Figure 1: We illustrate our method: we construct a series of neural networks with a manifold latent space. An intermediary Riemannian metric neural network is simulated with Ricci flow, in which we match the inner products of the tangents with the learned manifold with such a metric.

how the manifold evolves subject to the flow. Our method, captured by an intrinsic flow, is highlighted by this fact. This allows the manifold to displace through space, aside from the movements due to the flow, during its period of evolution. The embedding is irrelevant, and can change through the training procedure to maximize effectiveness in solving the objective function.

The intermediary stage of the parameterization domain acts similarly to the unstructured data in Euclidean space in the GD-VAE setting in the sense that it is fixed and with less structure than before its mapping to the manifold, except our parameterization domain is one dimension lower, being the intrinsic dimension, than the embedding dimension. The mapping from unstructured data to the manifold for GD-VAEs acts as a way to progress the encoding from data to that of a later state in the ambient data evolution. In our method, the dynamics in the manifold itself provide an accommodating manifold representation over the entire ambient PDE’s time interval, and the ambient PDE’s progression is learned in a larger scale of time by corresponding to a continuum.

While the implicitly-learned latent space captured by an intrinsic flow allows high precision in the task of replicating data from the same underlying distribution as seen as part of the training procedure, it is of interest to achieve precision in areas such as generalization of the data and extrapolation of data with fundamental qualities of those seen in training, but sufficiently different to be categorized as data that is extended outside of the training procedure. It is also of interest to develop methods that are highly robust against adversarial examples of test data, such as those corrupted with noise, given networks trained on dynamics of the original functions to be learned [29] [33] [1]. Many existing paradigms emphasize high performance on in-distribution data and not other such characteristics [24] [27] [1]. Our method focuses on advancing learning dynamics with the autoencoder paradigm. In particular, the manifold latent space with dynamics offers promise in extending data-based methods for learning PDEs from a baseline to one that not only produces high in-distribution performance, but also yields greater ability to infer dynamics from never-before-seen data, enhance robustness, as well as incorporate features of the data into such a structure [22].

2 Problem formulation

Problem setting. The task of interest is to learn the solution of a parameterized partial differential equation of the form

$$\partial_t \phi + \mathcal{D}_\alpha[\phi] = 0, \quad (1)$$

subject to initial data $\phi(\cdot, 0) = \phi_0$, where $\phi : \mathcal{X} \times [0, T] \rightarrow \mathbb{R}$ is the solution, and \mathcal{D}_α is a differential operator with parameter α . α may depend on evaluations over the input space \mathcal{X} as well as time $t \in [0, T]$. In particular, we seek a mapping

$$(\phi_0, t) \in C(\mathcal{X}; \mathbb{R}) \times [0, T] \rightarrow \phi_t \in C(\mathcal{X}; \mathbb{R}), \quad (2)$$

running over numerous instances of data. We devise an autoencoder framework, characterized by a latent space that consists of collections of points that lie directly along a continuum of manifolds $\mathcal{M}_{\hat{\tau}}$ embedded in Euclidean space \mathbb{R}^d , $\hat{\tau} \in [0, \tau]$ for some τ , to learn ϕ_t .

Ricci flow. Ricci flow is a natural framework for accomplishing goals of incorporating input data features into a manifold structure with generalization capability while allowing high precision in the task of producing the output. Ricci flow unites the separate features of an evolving latent space and a manifold latent space into a single scheme. Ricci flow is a partial differential equation that describes changes in the Riemannian metric. Let $g_{ij} : \mathcal{U} \times [0, \tau] \rightarrow \mathbb{R}$

be the components of the Riemannian metric matrix g over the manifold parameterization domain \mathcal{U} and a time domain $[0, \tau]$. Ricci flow is the metric evolution equation [34] [30]

$$\partial_t g(u, t) = -2\text{Ric}(g(u, t)), \quad (3)$$

for $u \in \mathcal{U}, t \in [0, \tau]$, such that the metric solved by 3 reflects that of the manifold $\mathcal{M}_{\hat{\tau}}$ over its respective time interval. The solution to this PDE can be regarded as an $m \times m$ matrix, $g(u, t)$, with components g_{ij} . The right-hand term $\text{Ric}(g(u, t))$ is the Ricci tensor. Ricci flow is similar to a geometric diffusion equation in which curvature is uniformized, and geometries contract or expand.

Metric coefficients. The coefficients of the Riemannian metric, g_{ij} , can be computed using the tangent vectors to the manifold at a location corresponding to a point in the manifold parameterization domain and time domain $\mathcal{U} \times [0, \tau]$. The coefficients of the metric can be computed at general times as [25]

$$g_{ij}(u, t) = \langle \partial_i \mathcal{E}(u, t), \partial_j \mathcal{E}(u, t) \rangle, \quad (4)$$

where ∂_ℓ is the component-wise partial derivative with respect to the ℓ -index in $u = (u^1, u^2, \dots, u^m)$ belonging to the parameterization domain \mathcal{U} , and $\mathcal{E} : \mathcal{U} \times [0, \tau] \rightarrow \mathbb{R}^d$ is the function mapping to the manifold continuum. We will hold $m = d - 1$. The Ricci flow PDE is primarily governed based on initial coefficients $g_{ij,0}$, but in our methodology, it of interest to compute the metric coefficients among arbitrary times $\tilde{\tau}_i \in U([0, \tau])$ in a uniform collocation procedure. The behavior of the manifold is governed by the change of the metric coefficients under Ricci flow such that equation 4 holds.

Ricci tensor. Given explicit knowledge of the Riemannian metric coefficients, one may compute the Ricci tensor using Christoffel symbols and the Riemannian curvature tensor. We have the collections of the Christoffel symbols, $\{\Gamma_{ij}^l\}_{i,j,l, 1 \leq i, j, l \leq m}$ evaluated at particular (u, t) [25], the Riemannian tensor $\{R_{i^l jk}^l\}_{i,l,j,k, 1 \leq i, l, j, k \leq m}$ [25], and the Ricci tensor $\{\text{Ric}_{ik}\}_{i,k, 1 \leq i, k \leq m}$ [7], given by

$$\Gamma_{ij}^l = \frac{1}{2} g^{kl} (\partial_j g_{ik} + \partial_k g_{ij} - \partial_i g_{kj}), \quad (5)$$

$$R_{i^l jk}^l = \partial_j \Gamma_{ik}^l - \partial_k \Gamma_{ij}^l + \Gamma_{ik}^p \Gamma_{pj}^l - \Gamma_{ij}^p \Gamma_{pk}^l, \quad (6)$$

$$\text{Ric}_{ik} = \text{Ric}(g(u, t))_{ik} = R_{i^l ik}^l. \quad (7)$$

We use Einstein notation, and so repeated indices in a term are summed. g^{kl} denote the elements of the inverse matrix of g at such a (u, t) . The Ricci tensor is a contraction of the Riemannian tensor, which is equivalently an analog of the trace of the Riemannian tensor. The above gives the corresponding Ricci tensor at a particular (u, t) .

3 Methodology

Ultimately, we seek a series of functions such that

$$\tilde{\phi}_t \approx (\mathcal{D} \circ \mathcal{E} \circ u)(\tilde{\phi}_0, t), \quad (8)$$

for approximate PDE data $\tilde{\phi}$, decoder \mathcal{D} , encoder \mathcal{E} , and parameterization u , parameterized by neural networks. The manifold, embedded in a low-dimensional space while subject to Ricci flow, is placed upon the encoding \mathcal{E} .

Neural network design. PDE solution information acts as input training data into a parameterization neural network u_{θ_u} , mapping such data to a point in the parameterization domain \mathcal{U} of the manifold continuum $\mathcal{M}_{\hat{\tau}}$. In particular, we construct a neural network $u : \mathbb{R}^N \times \Theta_u \rightarrow \mathcal{U}$, where data input is an N -dimensional vector containing data of the PDE initial condition discretization $\{\tilde{\phi}_0^i\}_i$, $\tilde{\phi}_0^i = (\phi^i(x_1, 0), \dots, \phi^i(x_N, 0))$, where x_j is in mesh Ω , and i is an index among the collection of training data. We denote $u_{\theta_u}(\tilde{\phi}) = u(\tilde{\phi}, \theta_u)$. The purpose of this neural network, instead of directly mapping PDE information into a manifold latent space, is so that the partial derivatives $\partial_i \mathcal{E}(u, t)$, hence tangent vectors, of the manifold may be taken with respect to the same domain in which the metric g is defined. Without this, 4 cannot be formulated, and the manifold cannot be learned in training.

We propose a physics-informed neural network (PINN) framework for finding the metric solution g to the Ricci flow equation. The PINN g_{θ_g} is constructed via standard neural network architecture, but is substituted into the pertinent PDE and is subsequently minimized as a PDE residual, as this is set to 0 in what should be satisfied [28] [36]

[13]. Differentiation of the PINN can be performed using automatic differentiation techniques found in deep learning libraries. To construct the metric, let $g : \mathcal{U} \times [0, \tau] \times \Theta_g \rightarrow \mathbb{M}^{m \times m}$, where $\mathbb{M}^{m \times m}$ is the set of $m \times m$ matrices. Since the metric should satisfy Ricci flow, the PDE residual to be minimized in our PINN setup is of the form [18]

$$\left\| \left\| \partial_t g_{\theta_g} + 2\text{Ric}(g_{\theta_g}) \right\|_F^2 \right\|_{L^1(\mathcal{U} \times [0, \tau])}. \quad (9)$$

Since the training loss runs over initial PDE data $\tilde{\phi}_0$, we will develop an analogous loss function with respect to this data.

Lastly, we construct encoder and decoder networks. The encoder maps a point along the learned parameterization domain directly onto the manifold embedded in Euclidean space at a specified time, and so the encoder additionally has a temporal input parameter corresponding to a state of evolution of the manifold. The encoder is given by $\mathcal{E} : \mathcal{U} \times [0, \tau] \times \Theta_{\mathcal{E}} \rightarrow \mathcal{M}_{\hat{\tau}}$. The decoder, $\mathcal{D} : \mathcal{M}_{\hat{\tau}} \times \Theta_{\mathcal{D}} \rightarrow \mathbb{R}^N$, maps the manifold point in Euclidean coordinates directly to known PDE solutions $\{\tilde{\phi}_t^i\}_i$ with training data given by

$$\bigcup_i \bigcup_{t \in \{j\Delta t, j \in \mathbb{N}, \Delta t \in \mathbb{R}^+\}} \{\tilde{\phi}_t^i = (\phi^i(x_1, t), \dots, \phi^i(x_N, t))\}, \quad (10)$$

but the framework can also be evaluated arbitrarily with respect to time if desired. The index i runs over numerous PDE solutions, and Δt is a time increment. A series of compositions of functions is taken to yield the final autoencoder output, with a loss restriction imposed at the intermediate step to ensure the desired evolution of Ricci flow is satisfied.

Loss function. We construct our training objective function as follows.

$$\theta = \arg \min_{\theta \in \Theta} \mathcal{L}_{Ric}(\theta) + \lambda_{dec} \mathcal{L}_{dec}(\theta) + \lambda_{met} \mathcal{L}_{met}(\theta) = \mathbb{E}_t \mathbb{E}_{\Phi} \left[\frac{1}{|\mathcal{U}|^2} \|\partial_t g_{\theta_g}(u, \tilde{\tau}) + 2\text{Ric}(g_{\theta_g}(u, \tilde{\tau}))\|_F^2 \right] \quad (11)$$

$$+ \lambda_{dec} \frac{1}{N} \|\mathcal{D}_{\theta_{\mathcal{D}}}(\mathcal{E}_{\theta_{\mathcal{E}}}(u, \hat{\tau})) - \tilde{\phi}_t\|_2^2 + \lambda_{met} \frac{1}{|\mathcal{U}|^2} \|g_{\theta_g}(u, \tilde{\tau}) - (J\mathcal{E}_{\theta_{\mathcal{E}}})^T J\mathcal{E}_{\theta_{\mathcal{E}}}\|_F^2 \Big]. \quad (12)$$

We use notation $u = u_{\theta_u}(\tilde{\phi}_0)$ and $J\mathcal{E}_{\theta_{\mathcal{E}}}$ to denote the Jacobian of vector $\mathcal{E}_{\theta_{\mathcal{E}}}$ with respect to u , i.e. $(J\mathcal{E}_{\theta_{\mathcal{E}}}(u, \tilde{\tau}))^T J\mathcal{E}_{\theta_{\mathcal{E}}}(u, \tilde{\tau}) = (J\mathcal{E}_{\theta_{\mathcal{E}}})^T J\mathcal{E}_{\theta_{\mathcal{E}}}$ is the matrix of inner products

$$(J\mathcal{E}_{\theta_{\mathcal{E}}})^T J\mathcal{E}_{\theta_{\mathcal{E}}} = \begin{pmatrix} \|\partial_1 \mathcal{E}_{\theta_{\mathcal{E}}}(u, \tilde{\tau})\|_2^2 & \langle \partial_1 \mathcal{E}_{\theta_{\mathcal{E}}}(u, \tilde{\tau}), \partial_2 \mathcal{E}_{\theta_{\mathcal{E}}}(u, \tilde{\tau}) \rangle & \dots \\ \langle \partial_2 \mathcal{E}_{\theta_{\mathcal{E}}}(u, \tilde{\tau}), \partial_1 \mathcal{E}_{\theta_{\mathcal{E}}}(u, \tilde{\tau}) \rangle & \|\partial_2 \mathcal{E}_{\theta_{\mathcal{E}}}(u, \tilde{\tau})\|_2^2 & \dots \\ \vdots & \vdots & \ddots \end{pmatrix}. \quad (13)$$

We motivate our loss so that the relation between the metric and the inner product of derivatives of 4 is satisfied under Ricci flow. A difference between decoder prediction and PDE solution is minimized to ensure a proper output.

The expectations run over time and the training data, taking data $\phi_0^i \sim \Phi$ for PDE data belonging to distribution Φ . We use notation $|\mathcal{U}| = \dim(\mathcal{U})$. To clarify, $\tilde{\phi}_t = \phi(\cdot, t)$ is the discretization of ϕ at time t . Let $\Theta = (\Theta_u, \Theta_g, \Theta_{\mathcal{E}}, \Theta_{\mathcal{D}})$. Let $\hat{\tau} \sim U(\{C_T i \Delta t : i \in \mathbb{N}, C_T, \Delta t \in \mathbb{R}^+\})$ be a uniform sampling on a scaling by constant C_T of the time domain $[0, T]$ discretized (generally $C_T = 1$), and let $\tilde{\tau} \sim U([0, \tau'])$ be uniformly sampled via a collocation procedure. We generally choose $\hat{\tau}, \tilde{\tau}$ to correspond by an identity relationship. Note that all times $t, \hat{\tau}, \tilde{\tau}$ are associated by some constant scaling. Hence, a time in the ambient PDE evolution has a corresponding time along the Ricci flow evolution to be decoded. The possible scaling of times helps facilitate a robust manifold representation, i.e. far in its evolution from a singularity. $\|\cdot\|_F$ is the Frobenius norm. All derivatives are computed via automatic differentiation [4]. The analytic expectations can be taken using empirical averages, additionally divided into batches with parameters updated with a stochastic optimizer [19].

The loss terms are organized as a Ricci flow physics-informed term \mathcal{L}_{Ric} , quadratic loss \mathcal{L}_{dec} to ensure the decoder matches the PDE solution, and a constraint term \mathcal{L}_{met} to match the manifold evolution with the metric satisfying Ricci flow. λ_{dec} and λ_{met} are scaling coefficients as needed (generally $\lambda_{dec} = \lambda_{met} = 1$). In the final term \mathcal{L}_{met} , g_{θ_g} is the matrix of the physics-informed metric term g_{θ_g} , where the components are summed with respect to each inner product $\langle \partial_j \mathcal{E}_{\theta_{\mathcal{E}}}, \partial_k \mathcal{E}_{\theta_{\mathcal{E}}} \rangle$ to enforce loss for each entry.

Special cases. Special cases of Ricci flow may be under consideration, which are favorable for reasons such as lower computational cost or higher-dimensional encodings. In these scenarios, information about the manifold is set

beforehand, such as the metric. Learned latent geometries are sacrificed at the gain of some other benefit. We discuss special cases in Appendix F. Coordinate transformations may be appropriate under select special cases. Our method in such a setting is discussed in Appendix E.

4 Experiments

We present Ricci flow-guided autoencoders on a series of numerical experiments for approximate solutions of PDEs given collections of known data. Our code is available at <https://github.com/agracyk2/Ricci-flow-guided-autoencoders-for-dynamics>. We compare our method to existing GD-variational autoencoder methods in [22], as well as other forms of autoencoder baselines. Results for both the Ricci flow method and alternative methods are collected using identical initial condition input spaces. The GD-VAE method is performed using an evolution mapping $\phi_t \rightarrow \phi_{t+\tilde{t}}$, where \tilde{t} is some time-increment. Predictions are retrained for new values of \tilde{t} . We emphasize our method needs no retraining for new t ; the latent manifold holds for all times in the ambient PDE.

The highlighting feature of our method is the manifold latent space subject to Ricci flow. We will reserve comparisons for recreating data as seen as part of the training procedure for manifold-based methodology to emphasize results for such a variety of framework.

1-d Burger's equation					
method	$t = 0$	$t = 0.25$	$t = 0.5$	$t = 0.75$	$t = 1$
Ricci flow	2.22 ± 1.31	1.51 ± 0.647	1.69 ± 0.754	1.50 ± 0.778	2.01 ± 1.04
GD-VAE	-	14.4 ± 18.9	4.52 ± 5.47	4.90 ± 6.88	3.75 ± 3.68
AE, g-proj.	-	10.3 ± 10.6	10.4 ± 7.89	5.29 ± 11.9	2.24 ± 1.13
1-d diffusion-reaction					
	$t = 0$	$t = 0.25$	$t = 0.5$	$t = 0.75$	$t = 0.9$
Ricci flow	0.274 ± 0.136	0.184 ± 0.0755	0.215 ± 0.0932	0.429 ± 0.199	1.14 ± 0.410
GD-VAE	-	2.10 ± 2.81	2.94 ± 6.17	1.53 ± 0.886	2.24 ± 0.881
AE, g-proj.	-	1.78 ± 2.59	1.28 ± 0.903	1.41 ± 0.595	2.77 ± 1.33
1-d diffusion-reaction extrapolation					
	$\mathcal{B}_{\text{diffusion}}^1, t = 0.35$	$\mathcal{B}_{\text{diffusion}}^2, t = 0.35$		$\mathcal{B}_{\text{diffusion}}^3, t = 0.35$	
Ricci flow	10.4 ± 15.4	17.8 ± 9.62		30.8 ± 13.1	
GD-VAE	14.9 ± 17.0	21.9 ± 13.9		36.1 ± 18.6	
AE	19.4 ± 27.0	23.6 ± 12.8		47.5 ± 26.3	
AE-extended	20.8 ± 31.6	21.7 ± 11.1		39.2 ± 15.6	
2-d Navier-stokes equation					
	$t = 0$	$t = 0.25$	$t = 0.5$	$t = 0.75$	$t = 1.0$
Ricci flow	4.44 ± 1.48	3.97 ± 1.57	5.26 ± 1.18	8.46 ± 1.09	9.25 ± 1.53
GD-VAE	-	84.3 ± 8.92	88.4 ± 12.8	93.5 ± 5.05	92.1 ± 4.02

Table 1: We compare our methodology to those existing, reporting relative L^1 errors on 30 testing sets. All errors are taken 10^{-2} . Times corresponding to the increment $\tilde{t} = 0$ are omitted for comparisons since this is a trivial learning task in these frameworks. Such error by a decrease in order of magnitude for the diffusion-reaction experiment has partial attribution to the enhanced MLP architecture (Appendix H).

4.1 Viscous Burger's equation

We first introduce our method on the viscous Burger's equation. The viscous Burger's equation is given by

$$\partial_t \phi(x, t) + \phi(x, t) \partial_x \phi(x, t) = \nu \partial_x^2 \phi(x, t), \quad (14)$$

for diffusion coefficient parameter $\nu \in \mathbb{R}$ [22].

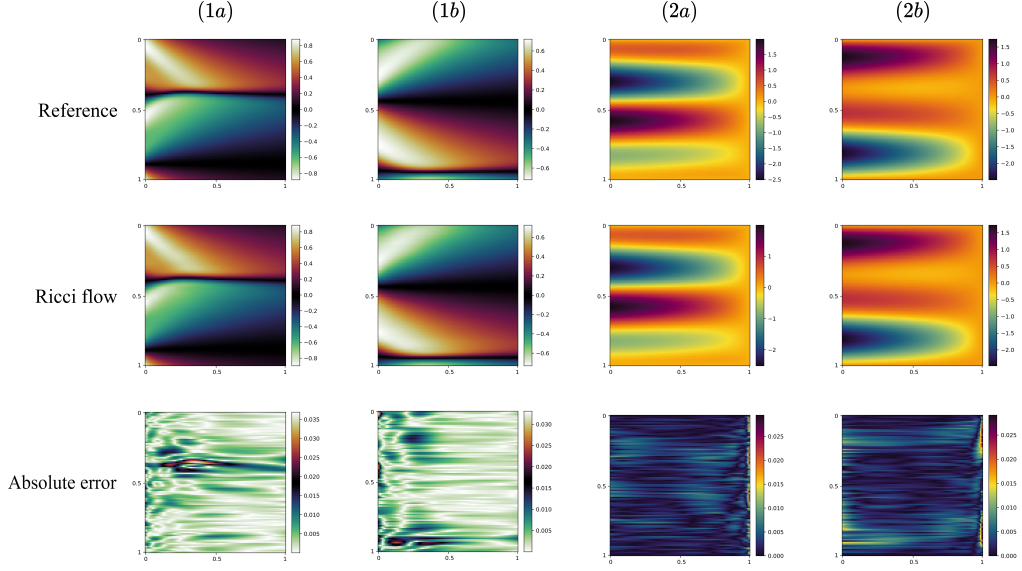


Figure 1: Illustration of numerical (1) Burger's equation and (2) diffusion-reaction solutions versus their Ricci flow solutions. (a) and (b) are two distinct solutions.

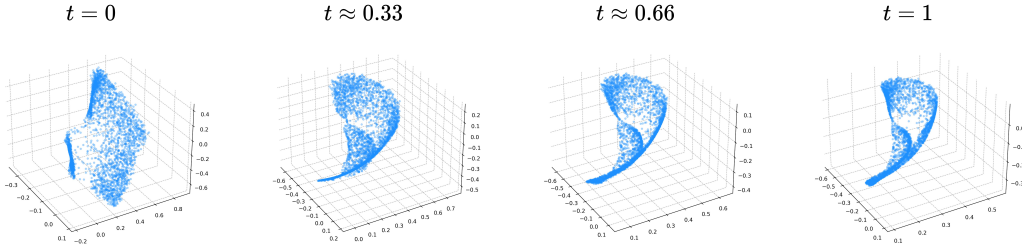


Figure 2: Illustration of the manifold latent space subject to Ricci flow in the Burger's equation experiment. The unusual behavior at $t = 0$ is potentially because it is a boundary, and is more difficult to learn. We provide an alternative view in Appendix K.

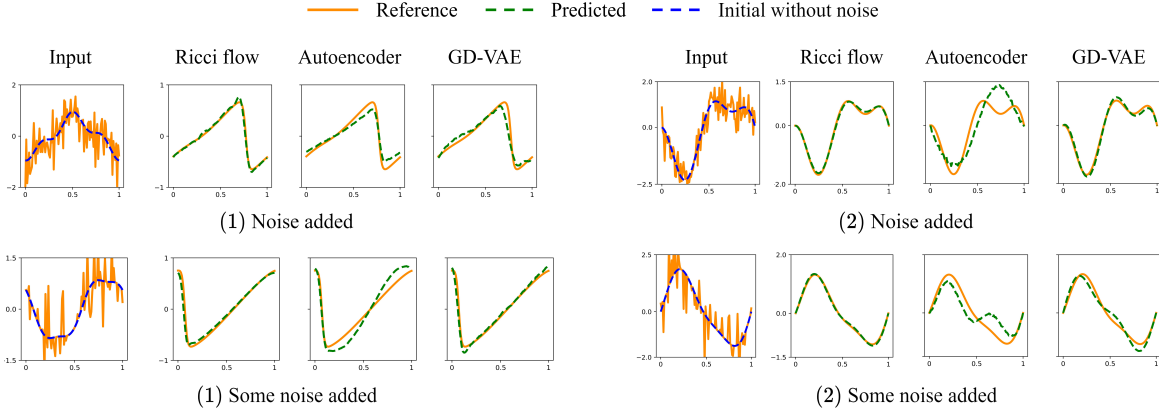


Figure 3: We compare methodology in the setting with injections of noise in the (1) Burger's equation and (2) diffusion-reaction experiments. We examine $t = 0.35$.

Our numerical evaluations for training and test data were constructed using a psuedo-spectral method with Fast Fourier transforms [5]. Evaluations were over a $(x, t) \in [0, 1] \times [0, 1]$ domain discretized into an equispaced grid $\Omega_x \times \Omega_t$ with mesh distance $h_x = h_t = 0.01$. Kinematic viscosity coefficient $\nu = 0.01$ was chosen. Initial conditions were evaluated from $\mathcal{A}_1 = \{\phi_0 : \phi_0 = \phi(x, 0) = \alpha \sin(2\pi x) + \beta \cos^3(2\pi x), \alpha, \beta \in [-1, 1]\}$. We choose training data by uniformly sampling 100 of ϕ_t for $t \in \Omega_t$ per each ϕ_0 . We set $\mathcal{U} \subseteq \mathbb{R}^m = \mathbb{R}^2$, and such a low dimension reduces computational cost.

Training consisted of a generation of 3,000 initial conditions. Loss coefficients $\lambda_{dec} = \lambda_{met} = 1$ were taken. We found training to occasionally be unstable, individuated by sudden increases in loss by orders of magnitude, resolvable by using a low learning rate, weight decay, and gradient clipping. The weight decay parameter was reduced in late training to ensure objective satisfaction.

Width of $w = 120$ was chosen for all neural networks in this experiment, which exhibited a balance of sufficiency and simplicity. All neural networks held 3 hidden layers. Experimentation for activation was upon both GELU(\cdot) [14] and tanh(\cdot), a choice of which was nonvital; however, we remark activation with sufficient continuous differentiability properties are necessary, as second order derivatives are taken to formulate the physics-informed Ricci flow.

We found success in taking sigmoid(\cdot) activation in the final layer of network u_{θ_u} , scaled by some arbitrary constant (we choose 2π). This forces the learned parameterization domain to be relatively small in measure, which allows highly nonzero partial derivatives to formulate the Riemannian metric from the manifold. This helps train both the manifold and the physics-informed network.

We examine our methodology on out-of-distribution cases belonging to the same training family, but with parameter deviations. We denote these sets as \mathcal{B} . In Figure 4, we give a comparison of our methodology, listing the changes made to the data. We list extrapolation error results in Table 3. Our extrapolation baselines are the GD-VAE framework, and a vanilla autoencoder with hyperparameters matching that of the Ricci flow setting when applicable, including a latent space of \mathbb{R}^3 . The AE g-proj. autoencoder as presented in [22] is the autoencoder baseline in the in-distribution test setting, maintaining consistency between manifold-based methods.

The AE-extended architecture is an autoencoder with exact architecture as our Ricci flow method, but without the latent manifold. This means we map to a \mathcal{U} once and subsequently low-dimensional Euclidean space (typically \mathbb{R}^3) before it is decoded. This comparison is meaningful because it removes error differences that are possibly from architecture, and we investigate performance differences due to the manifold and Ricci flow exactly. We remark we map to $\mathcal{U} \subseteq \mathbb{R}^3$ instead, as \mathbb{R}^2 fails to train, and we include sigmoid(\cdot) in the last layer for \mathcal{U} in this experiment only.

In Figure 3, we introduce noise to the data in a robustness experiment. We introduce Gaussian noise among all points in the discretization with variance $\sigma^2 = 0.5$, the set of which we denote \mathcal{C}^1 , and in sparse locations with $\sigma^2 = 0.75$, which we denote \mathcal{C}^2 . We found large learning rate (5e-4) had performance improvement in robustness in the GD-VAE setting in this experiment. We illustrate empirical error results corresponding to the same two scenarios in table 2. Refer to table 2 for comprehensive results on numerous instances of data, as figure 3 is too limited to present a wide overview of error analysis.

4.2 Diffusion-reaction equation

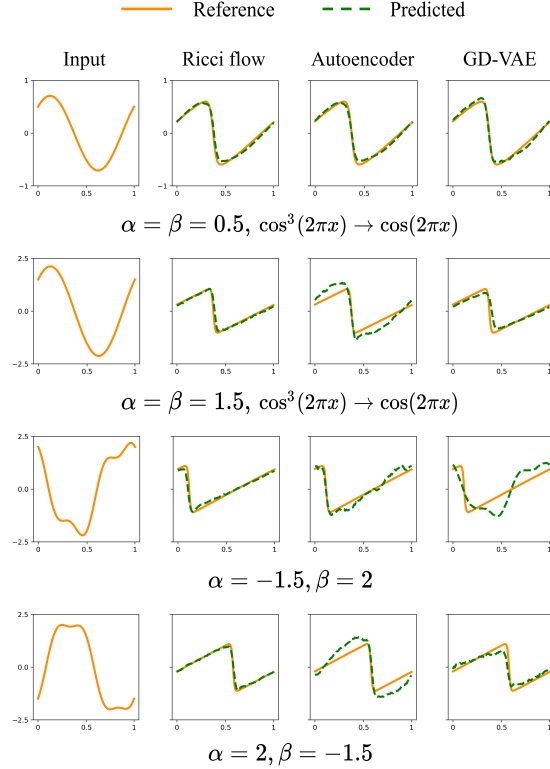


Figure 4: We compare various methodology in the extrapolation setting of out-of-distribution input data of varying difficulty for Burger’s equation. We examine $t = 0.35$.

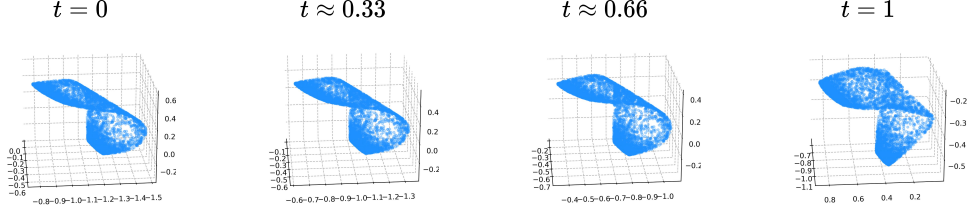


Figure 5: Illustration of the manifold latent space subject to Ricci flow in learning diffusion-reaction PDE data.

In this experiment, we study the setting of the 1-dimensional diffusion-reaction PDE with source term, given by the equation [38]

$$\partial_t \phi(x, t) = D \partial_x^2 \phi(x, t) + \lambda \phi^2(x, t) + f(x), \quad (15)$$

for diffusion coefficient $D \in \mathbb{R}$, reaction rate $\lambda \in \mathbb{R}$, and source term f . Our numerical scheme for constructing data was a finite difference solver [38]. Datasets were constructed over a $(x, t) \in [0, 1] \times [0, 1]$ domain. We choose mesh distance $h_x = h_t = 0.01$. We generated initial data from $f(x)$, using a special case of a Fourier series, $\mathcal{A}_2 = \{f : f(x) = \alpha \sin(2\pi x) + \frac{\alpha+0.5}{2} \cos(4\pi x) + \frac{\beta}{3} \sin(4\pi x), \alpha, \beta \in [-1, 1]\}$. The sum taken in the second coefficient ensures non-triviality of the initial data. Training data is normalized so that $\int_{\mathcal{X}} |\phi_0| dx = 1$, and the same scaling coefficient also scales data at time $t > 0$. We learn the mapping $(\phi_0, t) \rightarrow \phi_t$ despite initial functions being sampled for f and not ϕ_0 . Again, we set $\mathcal{U} \subseteq \mathbb{R}^m = \mathbb{R}^2$.

We implement an augmented architecture, the modified multilayer perceptron (MMLP), in this experiment, which has demonstrated success in physics-informed settings [38]. This architecture is elaborated upon in Appendix H, with training loss illustrated in Appendix 11, indicating this architecture achieves an order of magnitude lower training loss in fewer iterations of the Adam optimizer. In Table 4, our autoencoder baseline in the extrapolation setting uses the architecture used in the Ricci flow setting to allow fair comparison despite the baseline autoencoder being a non-physics-informed setting.

Training consisted of 5,000 samples from \mathcal{A}_2 paired with 100 uniformly sampled evaluations at later times $\phi_0(\cdot, t^*)$. Architecture consisted of 5 hidden layers for each network, a hidden layer being the term ζ^i as illustrated in Appendix H, which had a width of 100. GELU(\cdot) was used for all activations. We do not take sigmoid(\cdot) activation in the final layer of u_{θ_u} . We found the learned domain naturally has relatively small measure (see Appendix 17), hence sufficiently large derivatives. We reduced the latent dimension of the autoencoder baseline used in the extrapolation table of Table 4 to $d = 2$, but the autoencoder insufficiently solved the objective. This was done since $\mathcal{U} \subseteq \mathbb{R}^2$, but the inability to learn is not observed in our method. The autoencoder latent dimension \mathbb{R}^3 , our embedding dimension, is most applicable for comparison.

As with Burger’s equation, we provide an experiment with noise introduced into the data in various settings. We illustrate results in figure 3 and table 2.

4.3 Navier-Stokes equation

We test our method on the 2-d incompressible Navier-Stokes equation [9],

$$\partial_t v(x, t) + (v(x, t) \cdot \nabla) v(x, t) - \nu \nabla^2 v(x, t) = \frac{-1}{\rho} \nabla p(x, t), \quad (16)$$

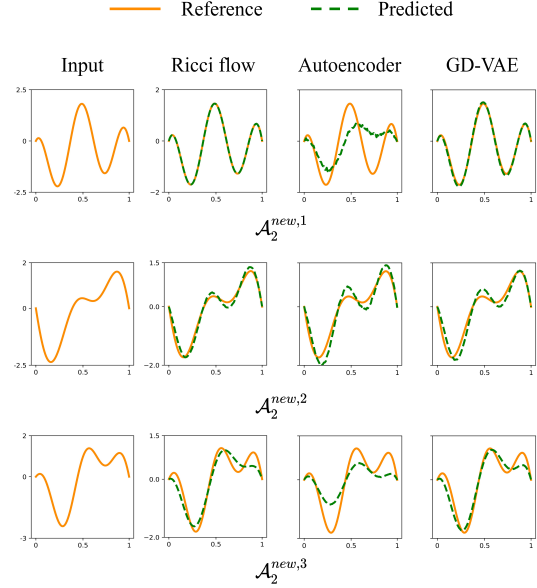


Figure 6: We compare various methodology in the extrapolation setting for the diffusion-reaction equation. We examine $t = 0.35$.

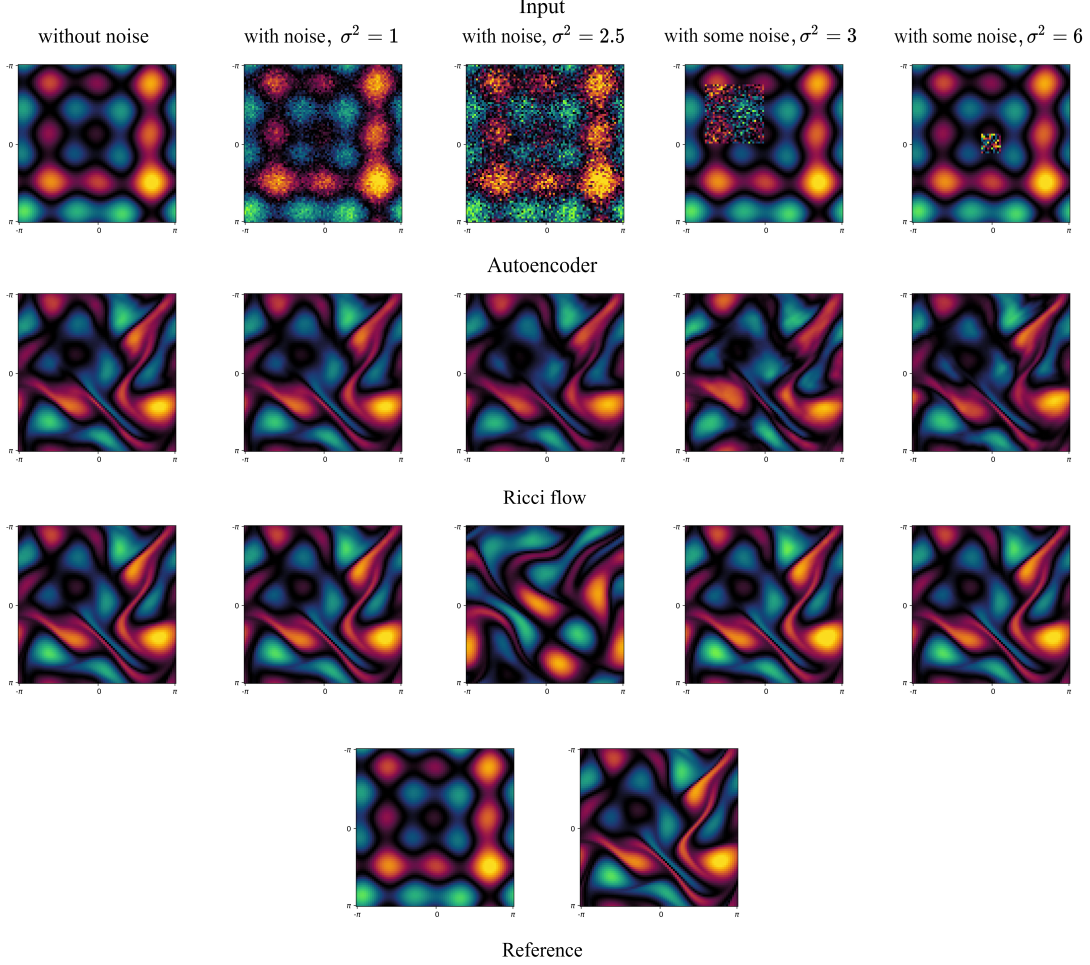


Figure 7: We illustrate results on the Navier-Stokes experiment at $t = 1$ with noise added using an autoencoder baseline. We set the seed for identical noise. As illustrated in section 4.3, we add noise to the various encoded stages, and not in the baseline. In particular, there is only one such stage for the baseline, and it is without structure, i.e. no manifold. We hold latent dimension $d = 100$ for the autoencoder, use similar architectures as to our method, and use dropout. Our method generally outperforms, but observe at $\sigma^2 = 2.5$, variance is sufficiently high that our method recognizes the solution to the input as a solution to an entirely different input.

given by the velocity field v evolution subject to the constraint $\nabla \cdot v = 0$, which is the incompressibility condition, and given an initial velocity vector field v_0 and pressure field over grid $\Omega_x \subseteq \mathcal{X} \subset \mathbb{R}^2$. The vorticity $\phi = \nabla \times v$ serves as training data, where $\nabla \times$ denotes the curl. We learn the autoencoder mapping $[(\nabla \times v_0)]_z \times t \rightarrow \phi_t$, where $[\cdot]_z$ is the z -th coordinate over Ω_x . Data for this experiment was constructed using a discontinuous Galerkin/Fourier spectral solver [9] [10].

We consider the special case of Ricci flow upon the $(d-1)$ -sphere. Data for this experiment consisted of 80×80 meshes in \mathbb{R}^2 , data of markedly higher dimensionality than in the previous experiments. A parameterization representation in \mathbb{R}^2 and an embedding in \mathbb{R}^3 were empirically found too limiting through dimensionality to thoroughly represent the data, and information was lost through such compression to accurately reconstruct solutions as well as provide prediction capacity. An encoding onto the $(d-1)$ -sphere allows for a dimension increase in \mathcal{U} and the embedding space \mathbb{R}^d by a reduction in the numerical power needed. While the manifold still evolves under a closed form of Ricci flow, the geometries are now fixed, but the latent expressivity is of enough importance to make the evolving $(d-1)$ -sphere more suitable.

A convolutional neural network (CNN) [26] was used for the parameterization network u_{θ_u} , taking 2-d grid input and mapping to $\mathcal{U} \subseteq \mathbb{R}^{100}$ for manifold parameterization. The $(d-1)$ -sphere was embedded in \mathbb{R}^{101} . We observed an artificial neural network gained greater empirical success over a transpose layer-based CNN for the decoder, achieving lower training error in fewer iterations of the Adam optimizer. Architecture for the decoder was taken as 101 – 400 – 1600 – 6400 – 6400 – (output), an architecture susceptible to overfitting. We applied techniques to prevent such, as described as follows. Wide architecture with severe overfitting regularization gained empirical favor over narrow architecture with modest regularization in the test setting.

Overfitting techniques were conducive towards generalization and accurately reconstructing solutions in the test setting. These techniques were notably dropout and adding Gaussian noise to the intermediate steps in producing the output, such as the parameterization space and the manifold in the embedded space [2]. Dropout was only used in the decoder, set in earlier layers as $p = 0.35$ and reduced before the final layer to $p = 0.25$. For the Gaussian noise, we first took a parameterization output $u \in \mathcal{U}$ and recast it as $u + C_{\xi^u} \cdot \xi^u$, where we use $[\xi^u]_i \sim \mathcal{N}(0, 1)$ to denote a tensor with standard normal elements $[\cdot]_i$ with the same dimensions as u . C_{ξ^u} denotes a scaling constant, which we took as 0.035. Gaussian noise was then added to manifold of the form $\mathcal{M} + C_{\xi^{\mathcal{M}}} \cdot r(\tau) \cdot \xi^{\mathcal{M}}$, instead scaling with the radius here and denoting $\xi^{\mathcal{M}}$ the analog of ξ^u for the manifold. We chose $C_{\xi^{\mathcal{M}}} = 0.075$. The multiplication with the radius ensures the Gaussian noise scales to prevent imbalance at lower radii.

The introduction of latent noise in this experiment acts similarly to a variational framework by transforming the latent space to a probabilistic setting, but training is not done with an ELBO-type loss, and the framework is missing desirable qualities that could otherwise be present at the gain of generalization. For example, the addition of noise comes at a sacrifice of structure, as the training data now lies in regions locally about but not on the manifold; however, the test data is evaluated without the addition of noise, and so test data is exactly along a manifold. Also, it cannot be guaranteed from this setting that similar instances of Navier-Stokes data share similar regions in the latent space, and such is a loss of identifiability. This is observable in figure 7, as severely-noisy ambient PDE data can be inferred as entirely different solutions.

Training data generation was costly for this experiment, taking about ~ 8 hours to generate 2200 solutions, 2000 for training and 200 for test. Such an increase in data is a less viable option to reduce overfitting, as it is often a limited option in practice.

The GD-VAE framework was established for this experiment using the architecture as presented in the repository, but width and depth were expanded to accommodate the increased difficulty of learning the data. Deep artificial neural networks were used for both the encoder and decoder. In practice, this methodology without heavy modification presented itself as unsuitable for this experiment, likely due to latent dimensionality.

1-d Burger's noise-added results		
method	$\mathcal{C}_{\text{Burger's}}^1, t = 0.35$	$\mathcal{C}_{\text{Burger's}}^2, t = 0.35$
Ricci flow	25.9 ± 20.0	12.4 ± 7.70
GD-VAE	49.7 ± 131	34.5 ± 40.6
AE	14.8 ± 6.64	15.6 ± 10.4
AE-extended	20.1 ± 10.2	22.6 ± 20.2

1-d diffusion-reaction noise-added results		
method	$\mathcal{C}_{\text{diffusion}}^1, t = 0.35$	$\mathcal{C}_{\text{diffusion}}^2, t = 0.35$
Ricci flow	18.6 ± 11.0	17.1 ± 9.48
GD-VAE	13.2 ± 7.68	13.6 ± 11.6
AE	63.6 ± 30.8	59.8 ± 37.9
AE-extended	44.5 ± 21.5	81.6 ± 81.4

Table 2: We examine relative L^1 error with initial data corrupted with noise on 30 test examples. Observe the Ricci flow method is fairly consistent among the methods. The high variances in the $\mathcal{C}_{\text{Burger's}}^1$ and $\mathcal{C}_{\text{diffusion}}^2$ settings are partially due to outliers (recall in the Burger's experiment, $\alpha, \beta \in [-1, 1]$, which allows near zero cases).

1-d Burger's extrapolation	
method	$\mathcal{B}_{\text{Burger's}}^1, t = 0.35$
Ricci flow	8.79 ± 4.84
GD-VAE	36.1 ± 17.8
AE	24.7 ± 20.3
AE-extended	40.4 ± 18.6

Table 3: We examine relative L^1 error for out-of-distribution data. We list $\mathcal{B}_{\text{Burger's}}^1$ in Appendix C.

5 Future work and limitations

Additional work could be created that seeks a method to incorporate extrapolation and noise data into the manifold in a more effective way. An implicitly-learned manifold undergoing dynamics would also be of consideration, in which such an accommodation could in turn improve such results even further.

[22] notes certain qualities such as periodicity work together with certain latent geometries. The concept of optimality of geometry could be further analyzed. One may attempt to quantify the question: how do deep neural networks harmonize well with data in a sense of geometry, particularly a geometric latent space?

Physics-informed Ricci flow is a nontrivial training task from a standpoint of computational difficulty. It is of interest to refine such a training algorithm to make this expedited and more practicable from the offline perspective.

6 Acknowledgments

We would like to thank Xiaohui Chen for helpful discussions in developing this project, particularly regarding intrinsic versus extrinsic geometric flows. Andrew Gracyk was supported by NSF under Grant No. 1922758 from DIGIMAT sponsorship. This research was based on work studied both before and after graduation from UIUC.

References

- [1] Abolaji D. Adesoji and Pin-Yu Chen. Evaluating the adversarial robustness for fourier neural operators, 2022.
- [2] Amir. Adding random noise to latent representation increase the accuracy in the autoencoder, answer, 2020. Licensed under CC BY-SA 3.0.
- [3] Arapura. M462 (handout 9).
- [4] Atilim Gunes Baydin, Barak A. Pearlmutter, Alexey Andreyevich Radul, and Jeffrey Mark Siskind. Automatic differentiation in machine learning: a survey, 2018.
- [5] Sacha Binder. Burgers’ equation simulation 1d (simulation de l’équation de burgers), 2021.
- [6] Sacha Binder. Wave equation simulations 1d/2d (équation de d’alembert), 2021.
- [7] Danny Calegari. Chapter 7: Ricci flow, 2023.
- [8] Qianying Cao, Somdatta Goswami, and George Em Karniadakis. Lno: Laplace neural operator for solving differential equations, 2023.
- [9] Daniel W. Crews. Incompressible2d, 2021.
- [10] Daniel W. Crews. Notes on the incompressible euler equation), 2021.
- [11] Alex Glyn-Davies, Connor Duffin, Ö. Deniz Akyildiz, and Mark Girolami. ϕ -dvae: Physics-informed dynamical variational autoencoders for unstructured data assimilation, 2023.
- [12] Somdatta Goswami, Aniruddha Bora, Yue Yu, and George Em Karniadakis. Physics-informed deep neural operator networks, 2022.
- [13] Zhongkai Hao, Songming Liu, Yichi Zhang, Chengyang Ying, Yao Feng, Hang Su, and Jun Zhu. Physics-informed machine learning: A survey on problems, methods and applications, 2023.
- [14] Dan Hendrycks and Kevin Gimpel. Gaussian error linear units (gelus), 2023.
- [15] hft. Tensor contraction criteria, answer, 2023. Licensed under CC BY-SA 3.0.
- [16] Xiang Huang, Zhanhong Ye, Hongsheng Liu, Beiji Shi, Zidong Wang, Kang Yang, Yang Li, Bingya Weng, Min Wang, Haotian Chu, Fan Yu, Bei Hua, Lei Chen, and Bin Dong. Meta-auto-decoder for solving parametric partial differential equations, 2022.
- [17] Olivier Hénot. The ricci flow equation, 2019.
- [18] Aarjav Jain, Challenger Mishra, and Pietro Liò. A physics-informed search for metric solutions to ricci flow, their embeddings, and visualisation, 2022.
- [19] Diederik P. Kingma and Jimmy Ba. Adam: A method for stochastic optimization, 2017.
- [20] Yangyang Li and Ruqian Lu. Applying ricci flow to high dimensional manifold learning, 2017.

- [21] Zongyi Li, Nikola Kovachki, Kamyar Azizzadenesheli, Burigede Liu, Kaushik Bhattacharya, Andrew Stuart, and Anima Anandkumar. Fourier neural operator for parametric partial differential equations, 2021.
- [22] Ryan Lopez and Paul J. Atzberger. Gd-vaes: Geometric dynamic variational autoencoders for learning nonlinear dynamics and dimension reductions, 2022.
- [23] Lu Lu, Pengzhan Jin, Guofei Pang, Zhongqiang Zhang, and George Em Karniadakis. Learning nonlinear operators via deepnet based on the universal approximation theorem of operators. *Nature Machine Intelligence*, 3(3):218–229, March 2021.
- [24] Hugo Melchers, Joost Prins, and Michael Abdelmalik. Neural green’s operators for parametric partial differential equations, 2024.
- [25] Richard S. Millman and George D. Parker. *Elements of Differential Geometry*. Prentice Hall, Inc., Englewood Cliffs, New Jersey 07632, 1977.
- [26] Keiron O’Shea and Ryan Nash. An introduction to convolutional neural networks, 2015.
- [27] Oded Ovadia, Vivek Oommen, Adar Kahana, Ahmad Peyvan, Eli Turkel, and George Em Karniadakis. Real-time inference and extrapolation via a diffusion-inspired temporal transformer operator (ditto), 2023.
- [28] Maziar Raissi, Paris Perdikaris, and George Em Karniadakis. Physics informed deep learning (part i): Data-driven solutions of nonlinear partial differential equations, 2017.
- [29] Bogdan Raonić, Roberto Molinaro, Tim De Ryck, Tobias Rohner, Francesca Bartolucci, Rima Alaifari, Siddhartha Mishra, and Emmanuel de Bézenac. Convolutional neural operators for robust and accurate learning of pdes, 2023.
- [30] Nick Sheridan. Hamilton’s ricci flow, 2006.
- [31] Jefferson Taft. *Intrinsic Geometric Flows on Manifolds of Revolution*. PhD thesis, University of Arizona, 2010.
- [32] Makoto Takamoto, Francesco Alesiani, and Mathias Niepert. Learning neural pde solvers with parameter-guided channel attention, 2023.
- [33] Pongpisit Thanasutives, Takashi Morita, Masayuki Numao, and Ken-ichi Fukui. Noise-aware physics-informed machine learning for robust pde discovery. *Machine Learning: Science and Technology*, 4(1):015009, February 2023.
- [34] Peter Topping. Lectures on the ricci flow, 2006.
- [35] Winfried van den Dool, Tijmen Blankevoort, Max Welling, and Yuki M. Asano. Efficient neural pde-solvers using quantization aware training, 2023.
- [36] Sifan Wang, Shyam Sankaran, Hanwen Wang, and Paris Perdikaris. An expert’s guide to training physics-informed neural networks, 2023.
- [37] Sifan Wang, Yujun Teng, and Paris Perdikaris. Understanding and mitigating gradient pathologies in physics-informed neural networks, 2020.
- [38] Sifan Wang, Hanwen Wang, and Paris Perdikaris. Learning the solution operator of parametric partial differential equations with physics-informed deepnets, 2021.
- [39] Tsung-Yen Yang, Justinian Rosca, Karthik Narasimhan, and Peter J Ramadge. Learning physics constrained dynamics using autoencoders. In S. Koyejo, S. Mohamed, A. Agarwal, D. Belgrave, K. Cho, and A. Oh, editors, *Advances in Neural Information Processing Systems*, volume 35, pages 17157–17172. Curran Associates, Inc., 2022.

A Navier-Stokes figure

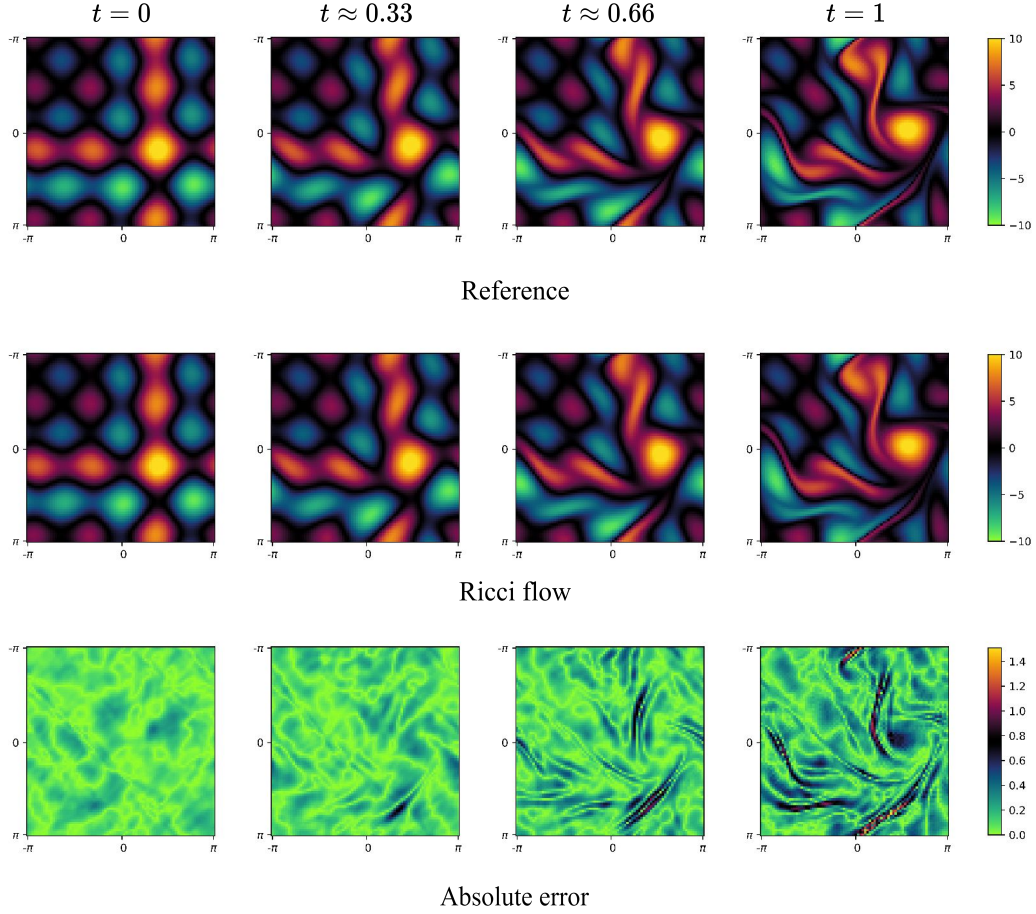


Figure 8: Comparison of numerical solution to our Ricci flow solution in the test setting on Navier-Stokes solution data.

B 2-d wave equation experiment

As a supplemental experiment, we deploy our Ricci flow-based method on learning the 2-d wave equation. A finite difference numerical scheme was used for constructing datasets for evaluation [6]. Neumann boundary conditions were used. A domain $\mathcal{X} = [0, 5] \times [0, 5]$ was used for space, with time in $[0, 4]$. Initial conditions were generated using a random Gaussian impulse of the form $\phi_0 = 10 \exp\{-\frac{(x-\mu_1)^2}{0.1} - \frac{(y-\mu_2)^2}{0.1}\}$, where $(\mu_1, \mu_2) \in U([1, 4] \times [1, 4])$ is uniformly random. 1,000 initial condition samples were used with 100 times taken for each initial sample for a training dataset of $1,000 \times 100 = 100,000$ solutions.

Training details were similar to that of the Navier-Stokes experiment of section 4.3. A convolutional neural network is taken for u_{θ_u} , mapping to $\mathcal{U} \subseteq \mathbb{R}^{100}$. The embedding is in \mathbb{R}^{101} . The special case of Ricci flow along the $(d-1)$ -sphere is employed. Unlike the Navier-Stokes experiment, overfitting techniques were unnecessary to achieve low empirical error in the test setting, where test data lies from the same underlying distribution as that of training. In particular, injections of noise into various stages of the neural network composition, and dropout, were not needed to achieve generalization in the testing phase. As with the Navier-Stokes experiment, a deep artificial neural network had performance gains over a deconvolutional neural network, taking an architecture of $101 - 400 - 1600 - 4600 - 4600 - (\text{output})$, where output is a 80×80 mesh of the PDE solution. The final output vector is unflattened to yield the desired grid.

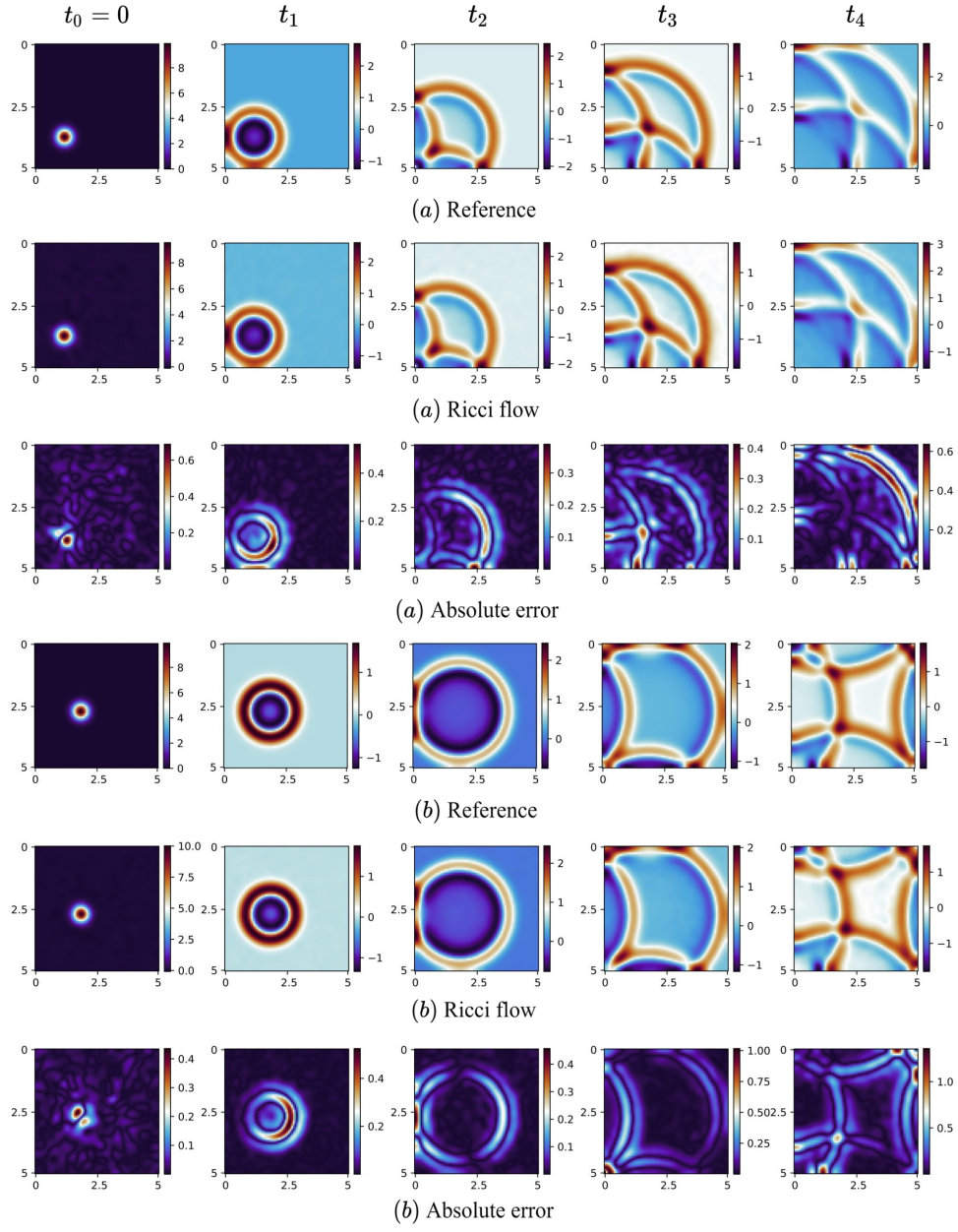


Figure 9: Comparison of numerical solution to our Ricci flow solution in the test setting on the 2-d wave equation. (a) and (b) represent two unique solutions.

C Extrapolation sets

We list the extrapolation set used in the Burger’s experiment. It is as follows:

$$\mathcal{B}_{\text{Burger's}}^1 = \{\alpha \sin(2\pi x) + \beta \cos(2\pi x) : \alpha, \beta \in [-1, 1]\} \cup \{(\alpha - 3\xi^1) \sin(2\pi x) + (\beta - 3\xi^2) \cos^3(2\pi x) : \quad (17)$$

$$\alpha, \beta \in [1, 2], \xi^{1,2} \sim \text{Bernoulli}(0.5), \xi^1 + \xi^2 > 0\}, \quad (18)$$

where an individual function is chosen from either set.

We list the extrapolation sets used in the diffusion-reaction experiment. They are as follows:

$$\mathcal{B}_{\text{diffusion}}^1 = \{\alpha \sin(2\pi x) + (\gamma + 0.5) \cos(4\pi x) + \beta \sin(4\pi x) : \alpha, \beta \in [-1.75, 1.75], \gamma \in [-1, 1]\}, \quad (19)$$

$$\mathcal{B}_{\text{diffusion}}^2 = \{\alpha \sin(2\pi x) + \frac{\alpha + 0.5}{2} \cos(\frac{7}{2}\pi x) + \frac{\beta}{3} \sin(\frac{7}{2}\pi x) : \alpha, \beta \in [0, 1]\}, \quad (20)$$

$$\mathcal{B}_{\text{diffusion}}^3 = \{\alpha \sin(2\pi x) + \frac{\alpha + 1}{2} \cos(\frac{9}{2}\pi x) + \frac{\beta}{3} \sin(\frac{9}{2}\pi x) : \alpha, \beta \in [0, 1]\}. \quad (21)$$

Data is normalized by $C = \int_{\mathcal{X}} |\phi_0| dx$ and scaled by C for all $t \in [0, 1]$ in this experiment.

D Training algorithm

Algorithm 1 Training algorithm

Input: Initial conditions $\{\tilde{\phi}_0^i\}_i$, solutions $\{\tilde{\phi}_{t_j}^i\}_{i,j}$ evaluated at $(x, t_j) \in \Omega \times [0, T]$

Setup: Sample $\hat{\tau}_i = C_T t_i$, sample $\tilde{\tau}_i \in U([0, \tau])$

- 1: **while** $\mathcal{L}(\theta)$ is not converged **do**
 - 2: Sample n initial conditions $\{\tilde{\phi}_0^i\}_{i \in \mathcal{I}_n}$ and n solutions $\{\tilde{\phi}_{t_j}^i\}_{i \in \mathcal{I}_n, j \in \mathcal{J}_n}$
 - 3: $u_i = u_{\theta_u}(\tilde{\phi}_0^i) \in \mathcal{U}$
 - 4: Compute encoded point on manifold $\mathcal{E}_{\theta_{\mathcal{E}}}(u_i, \hat{\tau}_j)$
 - 5: Compute decoded solution $\mathcal{D}_{\theta_{\mathcal{D}}}(\mathcal{E}_{\theta_{\mathcal{E}}}(u_i, \hat{\tau}_j))$
 - 6: Compute **Ricci flow loss**
-

Decoder loss

- 7: Compute $\mathcal{L}_{dec}(\theta)$ directly from decoder and $\{\phi^i(\cdot, t_j)\}$
-

Metric loss

- 8: Compute $\langle \partial_l \mathcal{E}_{\theta_{\mathcal{E}}}(u_i, \hat{\tau}_j), \partial_k \mathcal{E}_{\theta_{\mathcal{E}}}(u_i, \hat{\tau}_j) \rangle$
 - 9: Formulate $\mathcal{L}_{met}(\theta)$
-

Minimize objective.

- 10: Compute $\mathcal{L}_{Ric}(\theta) + \lambda_{dec} \mathcal{L}_{dec}(\theta) + \lambda_{met} \mathcal{L}_{met}(\theta)$
 - 11: Update θ
 - 12: **end while**
-

Algorithm 2 Ricci flow loss

Compute:

- 1: $\partial_t g_{\theta_g}(u_i, \tilde{\tau}_i)$
 - 2: $g^{kl} \in G^{-1}$
 - 3: $\partial_i g_{jk}$
 - 4: $\partial_{il} g_{jk}$
 - 5: $\Gamma_{ij}^l = \frac{1}{2} \sum_k g^{kl} (\partial_j g_{ik} - \partial_k g_{ij} + \partial_j g_{kj})$
 - 6: $R_{i^l jk} = \partial_j \Gamma_{ik}^l - \partial_k \Gamma_{ij}^l + \sum_p (\Gamma_{ik}^p \Gamma_{pj}^l - \Gamma_{ij}^p \Gamma_{pk}^l)$
 - 7: $\text{Ric}(g(u, t))_{ik} = \sum_l R_{i^l lk}$
 - 8: Loss $\mathcal{L}_{Ric}(\theta)$
-

E Coordinate transformations

We encourage the reader to flexibly consider special cases of manifolds in which Ricci flow may be applied. It may be of interest to transform the base coordinate system for such special case extensions. Let $(u^1, \dots, u^{m_u}) \rightarrow (v^1, \dots, v^{m_v}) : \mathcal{U} \rightarrow \mathcal{V}$ be a coordinate transformation from parameterization domains \mathcal{U} to \mathcal{V} . The Christoffel symbols indeed have a closed form under a coordinate transformation, but in order to evaluate Ricci flow in the \mathcal{V} based on the coordinates of \mathcal{U} , one only need consider the metric g and Ricci tensor $\text{Ric}(g)$. Denote $\tilde{g}_{\alpha\beta}$ the metric coefficients under \mathcal{V} . The metric under this coordinate transformation is [25]

$$\tilde{g}_{\alpha\beta} = g_{ij} \frac{\partial u^i}{\partial v^\alpha} \frac{\partial u^j}{\partial v^\beta}, \quad (22)$$

again using Einstein notation instead of summation notation. Denote $\widetilde{\text{Ric}}_{\alpha\beta}(g)$ the Ricci tensor in \mathcal{V} , and \tilde{R} the Riemannian tensor in \mathcal{V} . We will deduce the Ricci tensor under \mathcal{V} from the Riemannian tensor, which has a known form under a coordinate transformation [25]

$$\tilde{R}_{\alpha}{}^{\delta}{}_{\beta\gamma} = R_i{}^l{}_{jk} \frac{\partial u^i}{\partial v^\alpha} \frac{\partial v^\delta}{\partial u^l} \frac{\partial u^j}{\partial v^\beta} \frac{\partial u^k}{\partial v^\gamma}. \quad (23)$$

Einstein notation is here as well. Observe the Ricci tensor is a contraction, and so

$$\widetilde{\text{Ric}}(g)_{\alpha\gamma} = \tilde{R}_{\alpha}{}^{\delta}{}_{\delta\gamma} = R_i{}^l{}_{jk} \frac{\partial u^i}{\partial v^\alpha} \frac{\partial v^\delta}{\partial u^l} \frac{\partial u^j}{\partial v^\delta} \frac{\partial u^k}{\partial v^\gamma} = R_i{}^l{}_{jk} \tilde{\delta}_{jl} \frac{\partial u^i}{\partial v^\alpha} \frac{\partial u^k}{\partial v^\gamma}, \quad (24)$$

where $\tilde{\delta}_{jl}$ is the Kronecker delta, which follows from the chain rule and induces a contraction over indices (j, l) . Hence,

$$\widetilde{\text{Ric}}(g)_{\alpha\gamma} = R_i{}^l{}_{lk} \frac{\partial u^i}{\partial v^\alpha} \frac{\partial u^k}{\partial v^\gamma} = \sum_{i,k} \frac{\partial u^i}{\partial v^\alpha} \frac{\partial u^k}{\partial v^\gamma} \sum_l R_i{}^l{}_{lk}, \quad (25)$$

replacing Einstein notation with summation notation, giving the result

$$\widetilde{\text{Ric}}(g)_{\alpha\gamma} = \text{Ric}(g)_{ik} \frac{\partial u^i}{\partial v^\alpha} \frac{\partial u^k}{\partial v^\gamma}. \quad (26)$$

The step using $\tilde{\delta}_{jl}$ to form a contraction via the chain rule is noted in [15], which applies to the Ricci tensor under a coordinate transformation that we see here. Using the above, we can formulate Ricci flow in our objective function in terms of a transformed coordinate system using a Cartesian baseline.

Ricci flow under a coordinate transformation holds value when considering special cases of metrics under an alternative coordinate design over Cartesian coordinates. One may be interested in a manifold defined over a domain parameterized in Cartesian coordinates, which may offer certain computational advantages, while the metric coefficients or other useful properties of the manifold are governed by an alternative coordinate system.

We highlight such a closed form of the coordinate transformation as it is less familiar than other closed forms of transformations within literature, particularly literature relevant to deep learning. We refer the reader to [25] for other literature on coordinate transformations.

F Special cases

Special cases can be under consideration, which offer various advantages, the primary of which is reduction in computational power necessary to conduct the learning. This permits higher dimensional structures for more expressive representations. Specifications can be made that consolidate the possibilities of the manifold into a single structure, which generally constrain the problem, but also gain computational favor in the learning stage and yield possibly desirable results, especially if the manifold accords well with the PDE data.

Our special cases will be constraining the metric in one that is known, i.e. inherent to an exact and known manifold, using a known solution to Ricci flow via the manifold equation itself given a domain of parameterization, and a restriction to surfaces of revolution. One can extend special cases more generally, such as in using different coordinate systems, in which the result of Appendix E is useful.

F.1 Setting a known metric

In this setting, we specify a scenario with a known metric such that Ricci flow is satisfied. We will examine the cigar soliton, with initial metric given by

$$g_0 = g(u, 0) = \frac{du^1 \otimes du^1 + du^2 \otimes du^2}{1 + (u^1)^2 + (u^2)^2}, \quad (27)$$

which can be solved and extended for all times under Ricci flow. The cigar soliton metric for general times can be solved as in [17], which yields the metric

$$g(u, t) = \frac{du^1 \otimes du^1 + du^2 \otimes du^2}{e^{4t} + (u^1)^2 + (u^2)^2}. \quad (28)$$

This metric replaces the metric neural network g_{θ_g} implementation within the loss function, as well as the use of Ricci flow upon g_{θ_g} in the physics-informed setting. Now, we match the inner product of the tangent vectors upon $\mathcal{E}_{\theta_\varepsilon}$ with this fixed metric directly. Our optimization problem becomes the loss minimization framework

$$\min_{\theta \in \Theta} \mathbb{E}_t \mathbb{E}_\Phi \left[\frac{1}{N} \sum_j |\mathcal{D}_{\theta_{\mathcal{D}}, j}(\mathcal{E}_{\theta_\varepsilon}(u, \hat{\tau})) - \tilde{\phi}_{t,j}|^2 \right] \quad (29)$$

$$+ \mathbb{E}_t \mathbb{E}_\Phi \left[\frac{1}{2} \sum_{j=1}^2 |(e^{4\hat{\tau}} + \|u\|_2^2)^{-1} - \|\partial_j \mathcal{E}_{\theta_\varepsilon}(u, \hat{\tau})\|_2^2|^2 \right] \quad (30)$$

$$+ \mathbb{E}_t \mathbb{E}_\Phi [|\langle \partial_1 \mathcal{E}_{\theta_\varepsilon}(u, \hat{\tau}), \partial_2 \mathcal{E}_{\theta_\varepsilon}(u, \hat{\tau}) \rangle|^2]. \quad (31)$$

The first term is that to match the PDE solution, and the second and third are to enforce the cigar soliton manifold constraint. The loss function may be transformed for any fixed metric, generally minimizing the loss between the metric and $(J\mathcal{E}_{\theta_\varepsilon}(u, \hat{\tau}))^T (J\mathcal{E}_{\theta_\varepsilon}(u, \hat{\tau}))$, being the matrix of inner products of the tangent vectors, that we saw previously.

Another option is the torus, which has metric [18]

$$g(u, t) = (b + a \cos(u^2))^2 du^1 \otimes du^1 + a^2 du^2 \otimes du^2 \quad (32)$$

over domain $u^1 \times u^2 \in [0, 2\pi] \times [0, 2\pi]$. We will specify $b = 2, a = -1$. As with the cigar soliton, the matrix of the inner product of the tangent vectors can be matched with the fixed metric in training. A loss function similar to 29, 30 can be formulated with this metric; however, we remark this metric is independent of time, and the solution is learned purely by the displacement of the manifold through the embedding rather than through the flow.

One can enforce symmetry constraints upon the torus by the addition of the terms

$$\mathbb{E}_t \mathbb{E}_\Phi [|(J\mathcal{E}_{\theta_\varepsilon}(u^1, u^2, \hat{\tau}))^T (J\mathcal{E}_{\theta_\varepsilon}(u^1, u^2, \hat{\tau})) - (J\mathcal{E}_{\theta_\varepsilon}(u^1 + \delta, u^2, \hat{\tau}))^T (J\mathcal{E}_{\theta_\varepsilon}(u^1 + \delta, u^2, \hat{\tau}))|_F^2] \quad (33)$$

$$+ \mathbb{E}_t \mathbb{E}_\Phi [|(J\mathcal{E}_{\theta_\varepsilon}(u^1, u^2, \hat{\tau}))^T (J\mathcal{E}_{\theta_\varepsilon}(u^1, u^2, \hat{\tau})) - (J\mathcal{E}_{\theta_\varepsilon}(u^1, 2\pi - u^2, \hat{\tau}))^T (J\mathcal{E}_{\theta_\varepsilon}(u^1, 2\pi - u^2, \hat{\tau}))|_F^2] \quad (34)$$

to the loss, using the symmetry conditions for the torus $g(u^1, u^2, \hat{\tau}) = g(u^1 + \delta, u^2, \hat{\tau}), g(u^1, u^2, \hat{\tau}) = g(u^1, 2\pi - u^2, \hat{\tau})$ for $\delta \in [0, 2\pi]$ [18].

We present some computational results on the Burger's equation experiment in such settings. It is meaningful to compare to observe differences with geometry, as such acts as a means of displaying how different geometries produce different results.

1-d Burger's equation learning for fixed metrics					
method	$t = 0$	$t = 0.25$	$t = 0.5$	$t = 0.75$	$t = 1$
Cigar	1.38 ± 2.02	1.48 ± 1.38	1.62 ± 1.64	1.61 ± 1.88	2.17 ± 2.40
Torus	1.59 ± 0.969	2.49 ± 1.23	2.68 ± 1.31	2.46 ± 1.20	3.69 ± 2.49

Table 4: We examine our method on the Burger's equation experiment using the cigar soliton solution and the torus. All training details and hyperparameters are kept constant as those in the original experiment aside from the manifold learning.

1-d Burger's equation extrapolation	
Method	$\mathcal{B}_{\text{burger's}}^1, t = 0.35$
Cigar	15.5 ± 11.3
Torus	14.1 ± 5.76

Table 5: We examine extrapolation results on our fixed metrics on 30 test sets on Burger's equation data. Observe the standard deviation using the torus is significantly lower.

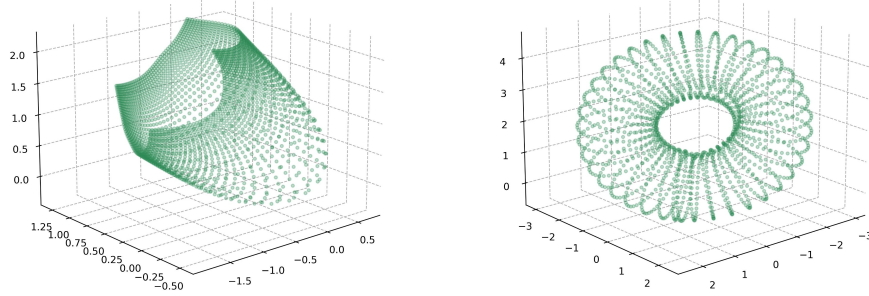


Figure 10: Examples of the cigar soliton and torus learned intrinsically in physics-informed settings. The metrics are fixed and we match the matrices of tangent vector inner products with the known metrics. This figure is purely illustrative, as the parameterization domains \mathcal{U} are fixed and not learned via a neural network as they would be by learning PDE data. Only the point of the cigar is learned, but the entire torus is learned.

F.2 $(d-1)$ -sphere

A manifold evolving according to Ricci flow can be known, in which employing the metric to solve the objective function can be avoided. We will turn our attention to the $(d-1)$ -dimensional sphere embedded in \mathbb{R}^d . The $(d-1)$ -sphere maintains that the fact that it is indeed a sphere subject to Ricci flow, while only the radius changes according to the equation

$$r(t) = \sqrt{R^2 - 2(d-2)t}, \quad (35)$$

for initial radius R [30]. The $(d-1)$ -sphere manifold parameterization is also known, and given by the parameterized equations

$$\mathcal{E}_{\mathbb{S}^{d-1}}^1 = r(t) \cos u^1, \quad \mathcal{E}_{\mathbb{S}^{d-1}}^i = r(t) \cos u^i \prod_{j=1}^{i-1} \sin u^j, \quad \mathcal{E}_{\mathbb{S}^{d-1}}^d = r(t) \prod_{j=1}^{d-1} \sin u^j, \quad (36)$$

where $i \in \{2, \dots, d-1\}$, and $(u^1, \dots, u^{d-1}) = u \in \mathcal{U}$ is still learned via a parameterization neural network u_{θ_u} . A decoder still maps the manifold points to the PDE solution, and so neural networks u_{θ_u} and $\mathcal{D}_{\theta_{\mathcal{D}}}$ remain while the metric network g_{θ_g} is removed, and the encoding network $\mathcal{E}_{\theta_{\mathcal{E}}}$ replaced.

Our objective function in this setting is greatly simplified, and becomes the risk minimization framework

$$\min_{\theta \in \Theta} \mathbb{E}_t \mathbb{E}_{\Phi} \left[\frac{1}{N} \sum_j |\mathcal{D}_{\theta_{\mathcal{D}},j}(\mathcal{E}(u, \hat{\tau})) - \tilde{\phi}_{t,j}|^2 \right]. \quad (37)$$

The inner product term is removed, as well as the Ricci flow term, which is automatically incorporated into the evaluation involving \mathcal{E} . This objective function reduces the PDE-solving problem to parameterizing the initial PDE data into the optimal point along the manifold, which evolves and is sequentially decoded.

Formulating the sphere with this method removes the fact that the evolution is governed by an intrinsic flow. In this special case, the sphere is centered at the origin, and so the embedding is fixed. The flow can be made to behave intrinsically in one of two ways.

The first way is to allow the sphere to shift the center away from the origin. This allows the evolution to behave similarly to how it would during an intrinsic flow. This can be done by constructing a new neural network $\mathcal{S}_{\theta_S} : [0, \tau] \times \Theta_S \rightarrow \mathbb{R}^d$, which displaces the sphere in the embedding based on time. This displacement is taken for all points along the sphere such that the center of the sphere is moved. This can be done using

$$\tilde{\mathcal{E}}_{\mathbb{S}^{d-1}}^i = \mathcal{E}_{\mathbb{S}^{d-1}}^i + \mathcal{S}_{\theta_S}^i, \quad (38)$$

where $\tilde{\mathcal{E}}$ is the new sphere after the change of centers. Observe $\mathcal{E}_{\mathbb{S}^{d-1}}$ is the fixed sphere at the center and \mathcal{S}_{θ_S} is learned in training. We denote i as the i -th coordinate in \mathbb{R}^d .

The second way is to utilize the known metric of the $(d-1)$ -sphere, and solve for the manifold with an encoding neural network as we did in F.1 via the inner product and metric relation. The metric of the $(d-1)$ -sphere is given as

$$g = r(t)^2 du^1 \otimes du^1 + r(t)^2 \sum_{i=2}^{d-1} \left(\prod_{j=1}^{i-1} \sin^2 u^j \right) du^i \otimes du^i. \quad (39)$$

F.3 Surfaces of revolution

Surfaces of revolution tend to pair well with periodic data, such as instances of periodicity corresponding to circular and torus-like topologies [22]. Furthermore by adding such a restriction and designing the neural networks in such a fashion to be suitable for a surface of revolution, computational gains are to be made, like with other special cases. While Ricci flow is an intrinsic flow, a manifold being a surface of revolution indeed is an extrinsic quality, in which our intrinsic methodology becomes one that is extrinsic in this special case.

A surface of revolution that is time-dependent is a manifold that takes the form

$$\hat{\mathcal{E}}(u^1, u^2, \hat{\tau}) = (r(u^1, \hat{\tau}) \cos(u^2), r(u^1, \hat{\tau}) \sin(u^2), z(u^1, \hat{\tau})). \quad (40)$$

In this framework, we bypass the need to parameterize an encoder and a metric, and instead we parameterize two neural networks

$$r_{\theta_r} = r : \mathcal{U}^1 \times [0, \tau] \times \Theta_r \rightarrow \mathbb{R}^+, \quad (41)$$

$$z_{\theta_z} = z : \mathcal{U}^1 \times [0, \tau] \times \Theta_z \rightarrow \mathbb{R}, \quad (42)$$

where $\mathcal{U}^1 \times \mathcal{U}^2 = \mathcal{U} \subseteq \mathbb{R}^2$ is the parameterization domain, and Θ_r, Θ_z are finite-dimensional parameter spaces.

A result proves that Ricci flow preserves symmetries found in the original metric g_0 and manifold \mathcal{M}_0 [7], meaning that a surface of revolution subject to Ricci flow maintains the fact that it indeed remains a surface of revolution throughout its evolution, i.e. symmetry is preserved. Such results in the fact that the form of equation 40 holds over its evolution. Furthermore, a surface of revolution has a fixed metric that is consequently known over this period, which is given by [25]

$$g = [(\partial_{u^1} r_{\theta_r}(u^1, \hat{\tau}))^2 + (\partial_{u^1} z_{\theta_z}(u^1, \hat{\tau}))^2] du^1 \otimes du^1 + r_{\theta_r}(u^1, \hat{\tau})^2 du^2 \otimes du^2, \quad (43)$$

using the neural networks in the metric. To solve Ricci flow, one need evaluate the Ricci tensor, which can be formulated from the Christoffel symbols which have a closed form under such a metric [3]:

$$\Gamma_{11}^1 = \frac{(\partial_{u^1} r_{\theta_r})(\partial_{u^1}^2 r_{\theta_r}) + (\partial_{u^1} z_{\theta_z})(\partial_{u^1}^2 z_{\theta_z})}{(\partial_{u^1} r_{\theta_r})^2 + (\partial_{u^1} z_{\theta_z})^2}, \quad (44)$$

$$\Gamma_{22}^1 = -\frac{r_{\theta_r} \partial_{u^1} r_{\theta_r}}{(\partial_{u^1} r_{\theta_r})^2 + (\partial_{u^1} z_{\theta_z})^2}, \quad (45)$$

$$\Gamma_{12}^1 = \Gamma_{21}^2 = \frac{\partial_{u^1} r_{\theta_r}}{r_{\theta_r}}, \quad (46)$$

$$\Gamma_{11}^2 = \Gamma_{12}^1 = \Gamma_{21}^1 = \Gamma_{22}^2 = 0. \quad (47)$$

Our training objective function is transformed into

$$\min_{\theta \in \Theta} \mathbb{E}_t \mathbb{E}_\Phi [|\partial_t(\partial_{u^1} r_{\theta_r}(u^1, \hat{\tau}))^2 + \partial_t(\partial_{u^1} z_{\theta_z}(u^1, \hat{\tau}))^2 + 2(\text{Ric}(g))_{11}|^2] \quad (48)$$

$$+ \mathbb{E}_t \mathbb{E}_\Phi [|\partial_t r_{\theta_r}(u^1, \hat{\tau})^2 + 2(\text{Ric}(g))_{22}|^2] + \mathbb{E}_t \mathbb{E}_\Phi [2(\text{Ric}(g))_{12}|^2 + |2(\text{Ric}(g))_{21}|^2] \quad (49)$$

$$+ \mathbb{E}_t \mathbb{E}_\Phi \left[\frac{1}{N} \sum_j |\mathcal{D}_{\theta_D, j}(r_{\theta_r}(u^1, \hat{\tau}) \cos(u^2), r_{\theta_r}(u^1, \hat{\tau}) \sin(u^2), z_{\theta_z}(u^1, \hat{\tau})) - \tilde{\phi}_{t, j}|^2 \right]. \quad (50)$$

To formulate the Ricci tensor, one can avoid analytic derivatives of the Christoffel symbols via automatic differentiation.

G Comparable methodology

The Riemannian tensor can additionally be computed using the coefficients of the second fundamental form [25], bypassing the need of Christoffel symbols. The coefficients of the second fundamental form are a collection $\{L_{ij}\}_{i,j=1}^{\dim(\mathcal{U})}$ defined as

$$L_{ij}(t) = \langle \partial_{ij}^2 \mathcal{E}(u, t), n(t) \rangle, \quad (51)$$

where \mathcal{E} is the manifold function taken with neural network $\mathcal{E} = \mathcal{E}_{\theta_{\mathcal{E}}}$, $u \in \mathcal{U}$ belongs to a parameterization domain, and ∂_ℓ denotes the partial derivative with respect to u^ℓ . n is the vector normal to the surface, i.e.

$$n(t) = \frac{\partial_1 \mathcal{E}(u, t) \times \partial_2 \mathcal{E}(u, t)}{\|\partial_1 \mathcal{E}(u, t) \times \partial_2 \mathcal{E}(u, t)\|_2} \quad (52)$$

when $\mathcal{U} \subseteq \mathbb{R}^2$. The Riemannian tensor can be formulated as

$$R_i^l{}_{jk} = L_{ik} L^l{}_j - L_{ij} L^l{}_k. \quad (53)$$

where we use

$$L^l{}_k = \sum_i L_{ik} g^{il}, \quad (54)$$

where the metric coefficients g_{ij} can be computed directly from the manifold \mathcal{E} as in equation 4. Hence, we can circumvent the use of a physics-informed neural network for the metric g_{θ_g} , and substitute the Riemannian tensor directly into the Ricci flow equation [20] for a residual. Ricci flow with the above formulation becomes

$$\partial_t \langle \partial_i \mathcal{E}, \partial_j \mathcal{E} \rangle = -2 \sum_l (L_{ij} L^l{}_l - L_{il} L^l{}_j). \quad (55)$$

where the indices (i, j) correspond to that that would be of the metric. The residual to minimize in the objective function to ensure the satisfaction of Ricci flow becomes

$$\mathcal{L}_{Ric}(\theta) = \mathbb{E}_t \mathbb{E}_{\Phi} \left[\sum_i \sum_j |\partial_t \langle \partial_i \mathcal{E}(u, \tilde{\tau}), \partial_j \mathcal{E}(u, \tilde{\tau}) \rangle + 2 \sum_l (L_{ij} L^l{}_l - L_{il} L^l{}_j)|^2 \right], \quad (56)$$

where the summation over (i, j) runs over the indices corresponding to the metric, and the summation over l runs over the contraction of the Ricci tensor with respect to the Riemannian tensor. The term $\mathcal{L}_{met}(\theta)$ is omitted in the loss minimization framework in this strategy.

This alternative methodology is comparable to that in which we previously established. It maintains approximate computational expense, distinguished by the amount of terms to be differentiated, and additionally requires a parameterization domain \mathcal{U} , typically low-dimensional to formulate the normal vector as a cross product; however, we remark it is worthy to realize what we formerly proposed can be reformulated in such a way, perhaps to be extended in future work.

H Augmented architecture

In this section, we describe the modified multilayer perceptron architecture as in [38] [37] for our diffusion-reaction experiment. Denote $\sigma(\cdot)$ a twice continuously differentiable activation function, and denote ζ neural network input. We first pass input ζ into two layers $\hat{\zeta} = \sigma(\tilde{W}\zeta + \tilde{b})$, $\tilde{\zeta} = \sigma(\tilde{W}\zeta + \tilde{b})$. The architecture proceeds iteratively as

$$\zeta^{i+1} = (1 - \sigma(W^i \zeta^i + b^i)) \odot \hat{\zeta} + \sigma(W^i \zeta^i + b^i) \odot \tilde{\zeta}, \quad (57)$$

where the first iterate is given by $\zeta^1 = \sigma(W^0 \zeta + b^0)$, and \odot denotes element-wise multiplication. Quantities W^i, b^i denote neural network weights and biases.

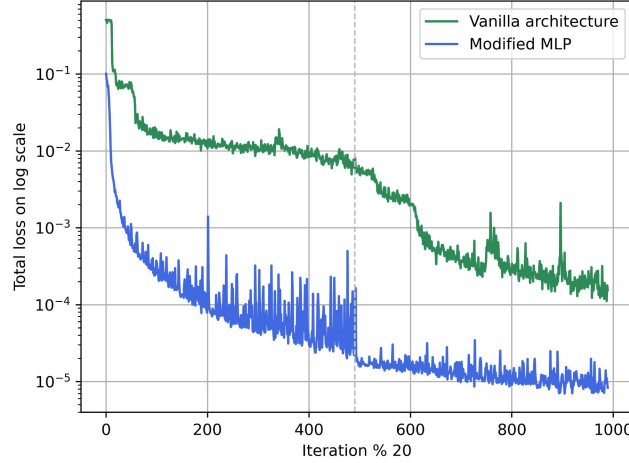


Figure 11: We compare training loss with the modified MLP architecture versus a vanilla architecture used in the diffusion-reaction experiment. The learning rate was adjusted after 10,000 iterations (dashed gray line). The first handful of iterations are omitted to better demonstrate the overall training.

I Additional experimental details

We assess our experiments using relative L^1 error upon predicted solutions and base data, using the metric

$$\mathbb{E}_{\Phi} \left[\frac{\|\mathcal{D}_{\theta_{\mathcal{D}}}(\mathcal{E}_{\theta_{\mathcal{E}}}(u, \hat{\tau})) - \phi_{\hat{t}}\|_{L^1(\mathcal{X})}}{\|\phi_{\hat{t}}\|_{L^1(\mathcal{X})}} \right], \quad (58)$$

at time \hat{t} corresponding to Ricci flow time $\hat{\tau}$, where an empirical average is taken to approximate the expected value. This metric behaves as a percentage error.

One way to facilitate the training process focuses on differentiation of the Christoffel symbols, i.e. $\partial_j \Gamma_{ik}^l$, which is nontrivial via automatic differentiation in a recurring training procedure, and adds significant time to the training process. This can mostly be resolved by differentiating each term involved in the Christoffel symbol calculation individually, and then forming the derivatives $\partial_j \Gamma_{ik}^l$ afterwards. This resulted in speeding up training by approximately $\times 3$ on a T4 GPU. When constructing our derivatives numerically, we first compute all second-order derivatives of the metric and then construct the Christoffel symbols from the derivatives of these terms via product rule, i.e.

$$\partial_j \Gamma_{ik}^l = \frac{1}{2} (\partial_j g^{pl} (\partial_k g_{ip} - \partial_p g_{ik} + \partial_i g_{pk}) + g^{pl} (\partial_{kj} g_{ip} - \partial_{pj} g_{ik} + \partial_{ij} g_{pk})). \quad (59)$$

J Empirical Ricci tensor evaluation

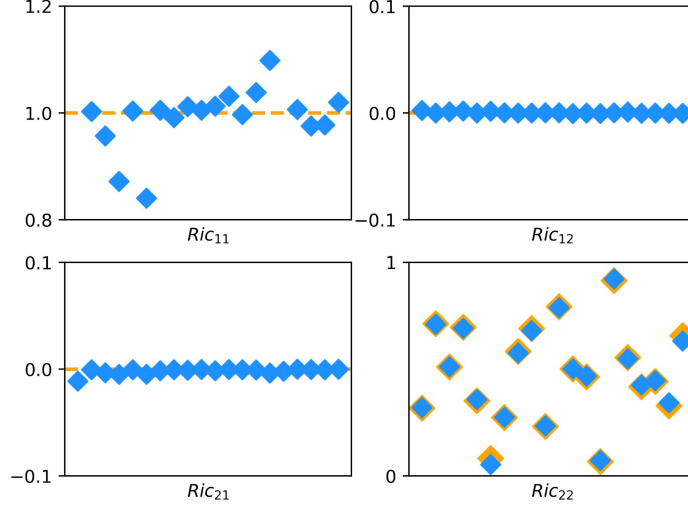


Figure 12: We demonstrate empirical results of our computed Ricci tensor (blue) compared to true Ricci tensor solutions (orange), where we learn the metric neural network g_{θ_g} upon the exact metric of the 2-sphere. It is known the Ricci tensor for the sphere with any radius is

$$\text{Ric} = (d - 1)g,$$

which is demonstrated in [30], where d is the intrinsic dimension here. g is the metric of the unit sphere. With $d = 2$, we have $g = du^1 \otimes du^1 + \sin^2(u^1) du^2 \otimes du^2$ (observe the radius is not here). Training is done on $(u^1, u^2, t) \in [0, \pi] \times [0, \pi] \times [0, 0.5]$ with radius = 1 at $t = 0$. The orange lines are at 0 for the (12), (21)-cases. For the (11), (12), (21)-cases, we evaluate the Ricci tensor within $[0.25, \pi/2]$ (we avoid $u^1 = 0$ because the metric tends to 0 elements here and is not invertible), and t is evaluated in a discretization $[0.1, 0.4]$ progressively along each point in the figure. The (22)-case is at $u^1 \in [0.25, \pi/2 - 0.25]$ and t is in the same discretization, and we plot the computed Ricci solution and the true $\sin^2(u^1)$. Note this experiment was conducted as Ricci tensor verification, and this experiment was not used to learn an ambient PDE.

K Alternative manifold views

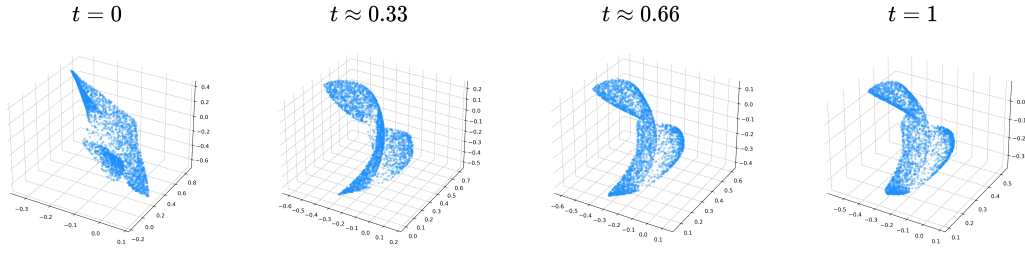


Figure 13: We provide an alternative view of the manifold as in the Burger's equation experiment.

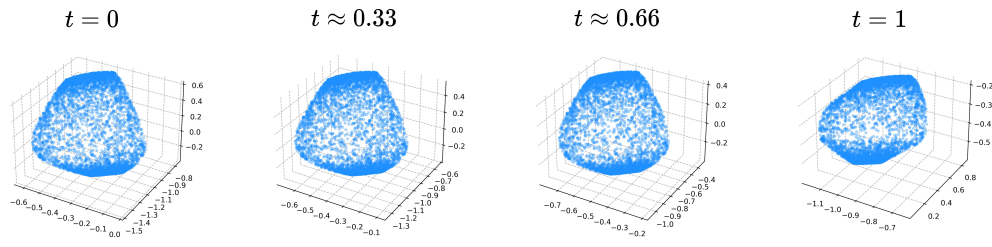


Figure 14: We provide an alternative view of the manifold as in the diffusion-reaction equation experiment.

L Additional figures

L.1 Burger's equation

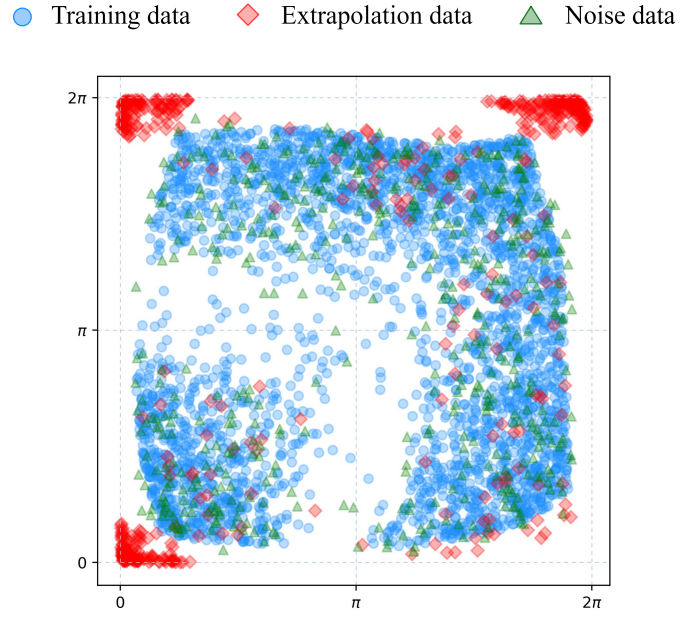


Figure 15: We view training, extrapolation, and noise data as points in parameterization domain \mathcal{U} .

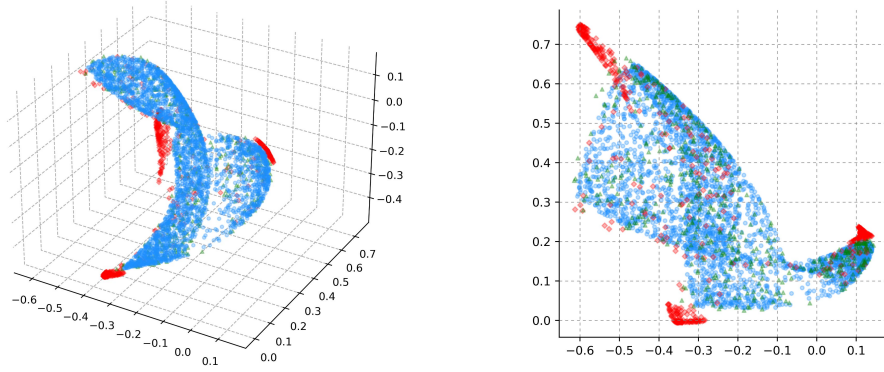


Figure 16: We view training, extrapolation, and noise data as points along the manifold at $t = 0.5$. The right image is a projection on the xy -axis.

L.2 Diffusion-reaction equation

● Training data ◆ Extrapolation data ▲ Noise data

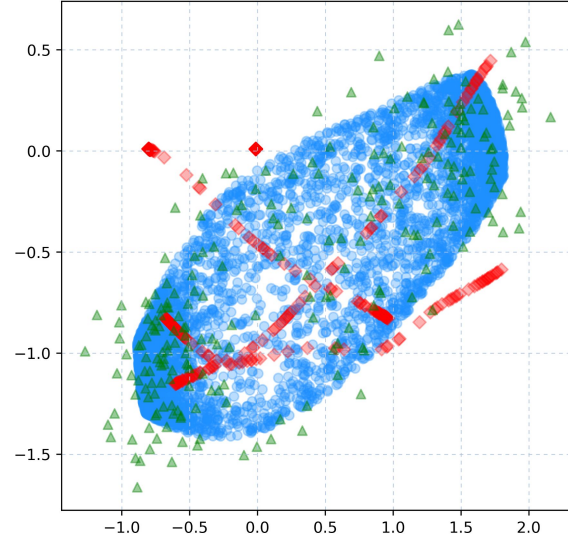


Figure 17: We view training, extrapolation, and noise data as points in parameterization domain \mathcal{U} .

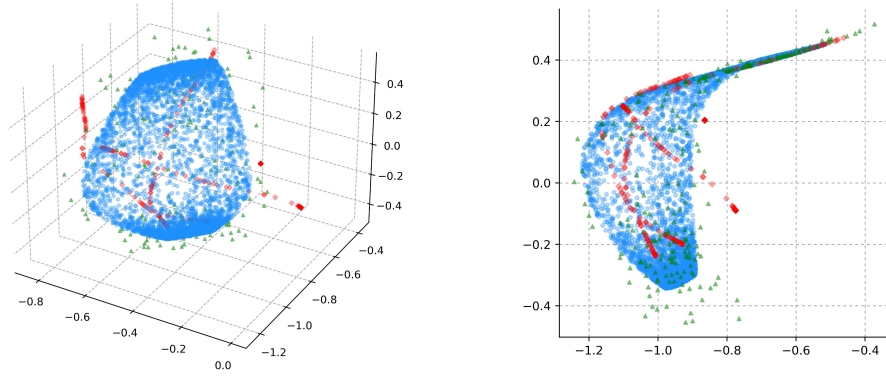


Figure 18: We view training, extrapolation, and noise data as points along the manifold at $t = 0.5$. The right image is a projection on the yz -axis.

M Additional wave equation figure

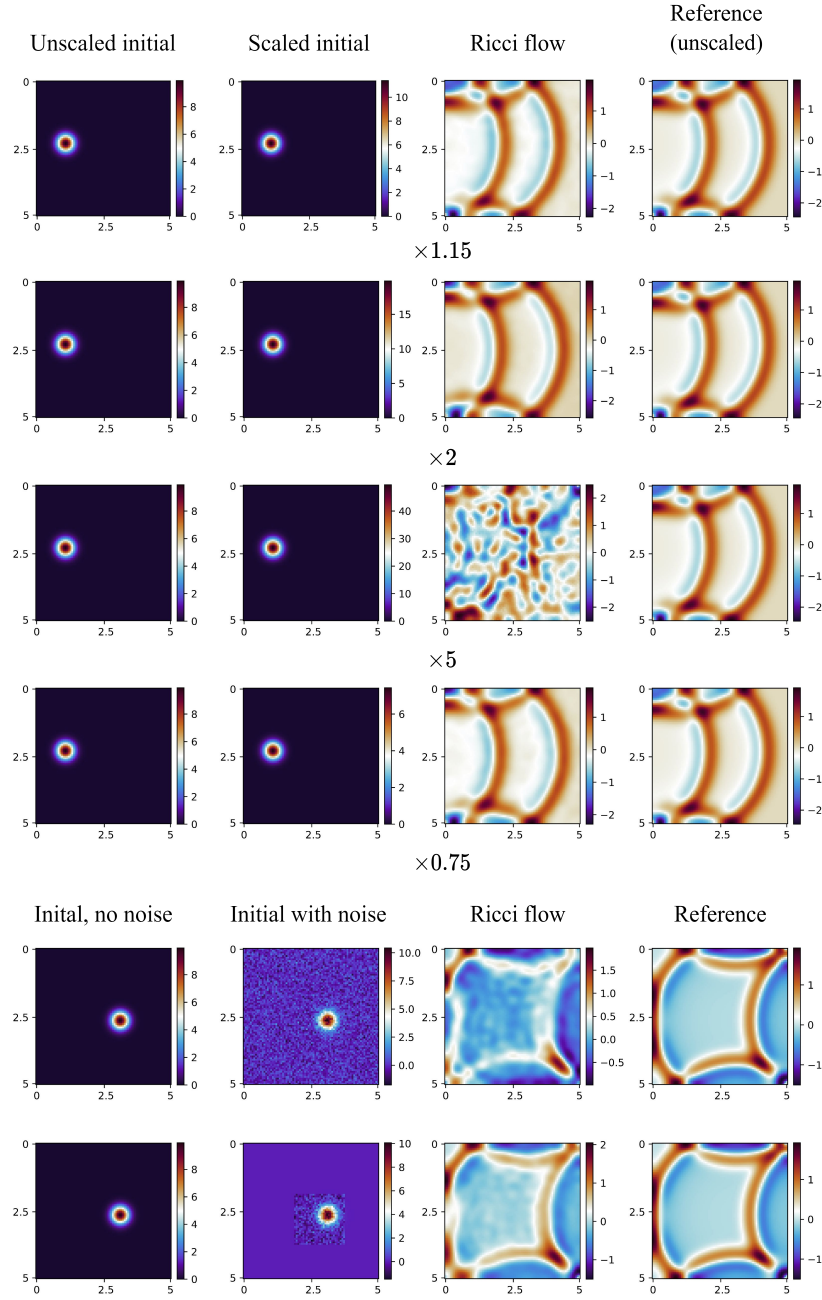


Figure 19: We present extrapolation and noise-injected robustness results on the wave equation experiment. The first four rows are on out-of-distribution data, with the initial impulse scaled by some constant. The last two are cases with noise introduced (variance of $\sigma^2 = 0.5$ for both).